The Institute for Solid State Physics
The University of Tokyo

ISSP

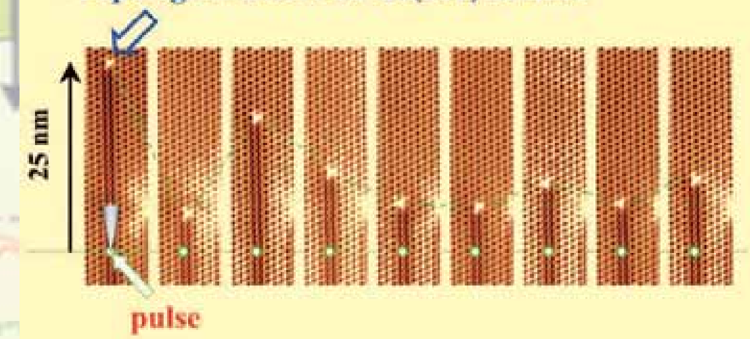

Activity Report
2005

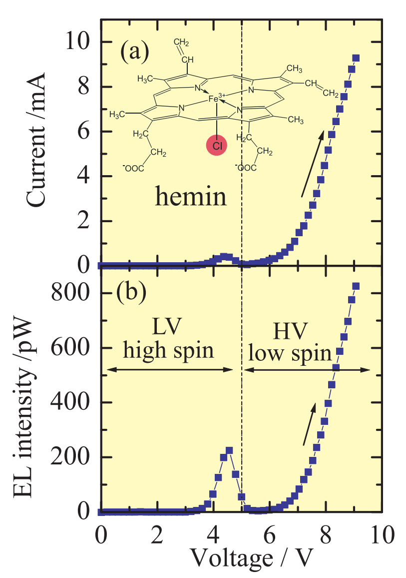

ISSP

Activity Report
2005

Contents

	Pages
Preface	1
Research Highlights	2 - 29
Highlights of Joint Research	30 - 44
ISSP Workshop	45 - 46
Proposal for Joint Research	47 - 84
Publications	85 - 122

Preface

The ISSP was established in 1957 based on the recommendation of the National Council of Japan to set up a new institute for condensed matter physics. The idea was to establish a top class research institute for experimental and theoretical studies of condensed matter and to promote cooperative research in the field throughout the country. Soon after the inauguration, the name of ISSP became recognized world-wide in the community of condensed matter physics.

Since then there have been two major changes in the history of the institute. The first was the reorganization of the institute in the mid-eighties. The system of divisions consisting of several groups was introduced and the project of the "Physics in extreme conditions", which includes Ultra-High Magnetic Fields, Laser Physics, Surface Physics, Ultra-Low Temperatures, and Very High Pressures, was started. The second major change was the relocation of the ISSP to the new Kashiwa campus which was completed in 2000.

To make the status of the research activities in the ISSP public, new forms were introduced in 2001: Activity report A for research mostly by the staff of the ISSP and Activity report B for joint research conducted by the ISSP. This copy is the Activity Report for the fiscal year 2005 in the style of single volume for all the research activities at the ISSP. The system of national universities in Japan has made a profound change from April in 2004 by the so called "houjinka", which means that national universities, once directly belonged to the ministry of education, have become independent administrative entities. In the new scheme importance of the Activity Report has been increased.

We are happy to receive any comments on the Report for the possible improvement of the research activities of the ISSP.

June 21, 2006
Kazuo Ueda
Director
Institute for Solid State Physics
The University of Tokyo

Research Highlights

Pressure Effect on Superconductivity and Antiferroquadrupolar Order in $PrOs_4Sb_{12}$

Sakakibara Group

Heavy-fermion (HF) behavior occurs in a variety of Ce-, U-, or Yb-based compounds, but less is known for the Pr-based compounds where doubly occupied *f* electrons are much more localized. Thus, Pr-based filled skutterudites have attracted a considerable amount of attention in recent years because they offer unique opportunities for exploring the HF behavior. Unlike the Ce-, U-, or Yb-based compounds, most of Pr-based filled skutterudites have a nonmagnetic ground state in the crystalline electric field (CF). Hence, its HF behavior has often been discussed in terms of the interaction between the electric quadrupolar moments of Pr^{3+} and conduction electrons.

Here we report on our recent magnetization study on the HF superconductor $PrOs_4Sb_{12}$ (T_{c1}=1.85 K and T_{c2}=1.75 K) under pressure. This compound exhibits an antiferroquadrupolar (AFQ) transition in high fields above 45 kOe, in addition to superconductivity. The occurrence of the field-induced AFQ transition can be understood in terms of a level-crossing of a Γ_1 singlet ground state and a Γ_4 triplet excited state located at Δ=8 K. Recent inelastic neutron-scattering experiments have revealed that low-energy excitations are mainly due to nonmagnetic quadrupolar interactions associated with the AFQ order. It is also suggested that occurrence of HF superconductivity in this compound is closely related to the quadrupolar excitons, although it is still unclear how the quadrupolar excitons affect the superconducting state. Recently, it is theoretically shown that T_c strongly depends on the magnitude of the energy splitting Δ in a multipole-exciton-mediated superconductivity scenario. Hence, pressure experiment becomes very important, because pressure dependence of T_c and Δ enables to clarify the relationship between superconductivity and the quadrupolar excitons.

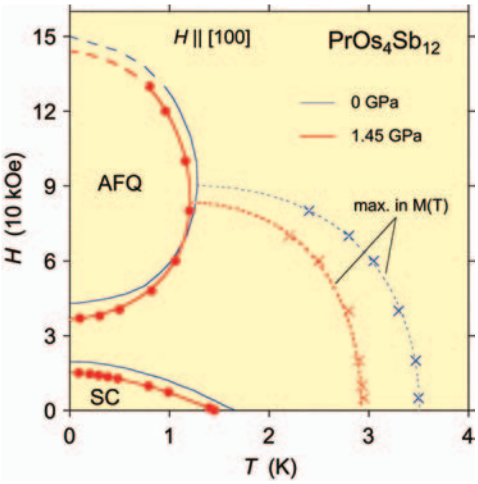

Fig. 1. *H*-*T* phase diagram of $PrOs_4Sb_{12}$ deduced from magnetization measurements. The blue and red lines are obtained from the data at 0 and 1.45 GPa, respectively. For the two superconducting transitions, only the phase boundary for T_{c2} is shown. The crosses represent the temperature where the *T*-dependence of the magnetization exhibits a maximum. The dashed lines are a guide to the eye. SC: superconducting state and AFQ: antiferroquadrupolar ordered state.

Figure 1 shows the magnetic phase diagram of $PrOs_4Sb_{12}$, as deduced from the present magnetization measurements. The blue and red lines represent the data at P=0 and 1.45 GPa, respectively. For the superconducting (sc) phase, only the phase boundary for T_{c2} is shown. The phase diagram clearly indicates that the sc region decreases with an increase in pressure. On the other hand, the AFQ ordered phase moves to lower fields as the pressure increases, while its area remains almost the same. The crosses indicate the temperature T^* at which the $M(T)$ curve becomes maximum, and the dashed lines are fits to the T^* data. The T^*(H) line at P=0 approaches a point where T_Q is the largest. Similar behavior is observed in the $T^*(H)$ line at 1.45 GPa. Analysis of our experimental data on the CF model reveals that the CF energy splitting Δ between the Γ_1 and Γ_4 states decreases with an increase in pressure, whereas the two sc transition temperatures decrease significantly. Therefore, the observations raise a question about the scenario for superconductivity mediated by the quadrupolar excitons alone.

Inelastic neutron scattering experiments have revealed that quadrupolar excitons dominate low-energy excitations in $PrOs_4Sb_{12}$, indicating that quadrupolar interactions must be relevant in the sc state. The present phase diagram demonstrates that the sc region decreases with increasing pressure, although the AFQ phase approaches the sc phase. Such behavior can be expected to occur when the quadrupolar interactions associated with the AFQ order suppress superconductivity. Thus, our data suggests that the sc state competes with the AFQ ordered state.

References

[1] T. Tayama, T. Sakakibara, H. Sugawara, and H. Sato, J. Phys. Soc. Jpn. **75**, 043707 (2006).

Authors
T. Tayama, T. Sakakibara, H. Sugawara[a], and H. Sato[b]
[a]The University of Tokushima
[b]Tokyo Metropolitan University

A Voltage-Induced Transition of Hemin in BIODE (Biomolecular Light-Emitting Diode)

Tajima and Akiyama Groups

A thin-film organic light-emitting diode (OLED) was fabricated by Vincett *et al.* for the first time [1]. This device is of interest not only for the practical use but also for the basic research. By fabricating this device, we can measure electro-luminescence (EL) spectra of insulating organic compounds, and can study their electrical and optical properties simultaneously. We recently succeeded in obtaining the EL spectra of cytochrome *c* [2]. This is the first report on the fabrication of the biomolecular light-emitting diode ("BIODE"). Subsequently, we fabricated BIODE devices using other porphyrin-containing biomolecules (myoglobin [3], chlorophyll *a* [4]) and reported the EL spectra of the compounds. Interestingly, heme proteins (heme = iron porphyrin) do not or hardly exhibit photoluminescence (PL), although chlorophyll *a*, which does not contain iron, exhibits PL. In this respect, the mechanism of EL in heme proteins is of interest not only for bioscience but also for physics [5].

Hemin is a small molecule containing an iron protoporphyrin IX unit (see the inset of Fig. 1a). This compound does not exhibit PL. Figure 1a and 1b show the current and EL intensity simultaneously measured for a hemin BIODE [6]. The two characteristics are plotted as a function of the biased voltages applied to the electrodes. Interestingly, both characteristics took a peak above V=4 V. Similar behavior was observed in other samples, suggesting a voltage-induced transition. Hereinafter, we call the state before the transition as the low-voltage (LV) state and the state after the transition as the high-voltage (HV) state, respectively. The voltage-induced transition was irreversible.

In order to examine the origin of the transition, we measured the EL spectra in both LV and HV state. Figure 2 shows the EL spectra [6]. The EL spectrum of hemin in the LV state is composed of several narrow bands, while the spectrum in the HV state exhibits broad peaks. The spectral features in the HV state are very similar to those of cytochrome *c* and myoglobin.

The spectral changes associated with the applied voltages remind us of the transition from a low-spin state into a high-spin state in the compounds containing iron porphyrins. The native form of cytochrome *c* is a low-spin compound of iron. Both the high-spin and low-spin states are known in myoglobin. Hemin is a high-spin five-coordinate compound of iron. However, the spin state of these compounds is very subtle and easily changes when the substitution or addition of ligands occurs. Thus in order to ascertain the spin state of the compounds used for the device fabrication, we measured the magnetic susceptibility, Raman spectra of the compounds [6]. After the measurements, we concluded that the broad feature of the electroluminescence is characteristic for iron porphyrin in the low-spin state, and that hemin in the LV state is in the high-spin state while hemin in the HV state is in the low-spin state.

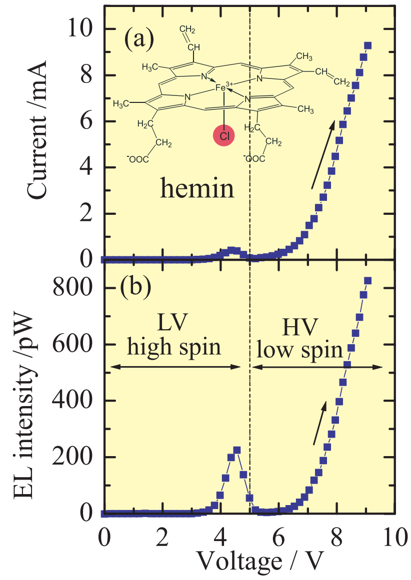

Fig. 1. (a) Current-voltage, and (b) EL intensity-voltage characteristics of an ITO/hemin/Al junction. The inset shows the molecular structure of hemin. The broad peak around 4.5 V is due to the voltage-induced transition [6].

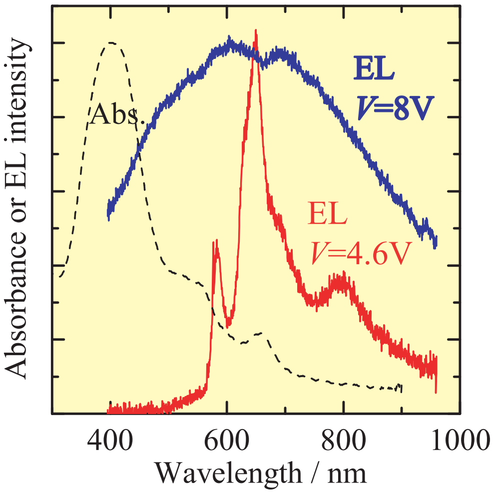

Fig. 2. The EL and absorption spectra of hemin. The EL spectrum in the low-voltage state (red curve) is attributable to hemin in the high-spin state, while that in the high-voltage state (blue curve) is associated with hemin in the low-spin state [6].

References

[1] P. S. Vincett, W. A. Barlow, R. A. Hann, and G. G. Roberts, Thin Solid Films **94**, 171 (1982).

[2] H. Tajima, S. Ikeda, M. Matsuda, N. Hanasaki, J. Oh, and H. Akiyama, Solid Sates Commun. **126**, 579 (2003).

[3] H. Tajima, S. Ikeda, K. Shimatani, M. Matsuda, Y. Ando, J. Oh, and H. Akiyama, Synth. Met. **153**, 29 (2005).

[4] K. Shimatani, H. Tajima, T. Komino, S. Ikeda, M. Matsuda, Y. Ando, and H. Akiyama, Chem. Lett. **34**, 948 (2005).

[5] S. Ikeda, H. Tajima, M. Matsuda, Y. Ando, and H Akiyama, Bull. Chem. Soc. Jpn. **78**, 1608 (2005).

[6] H. Tajima, K. Shimatani, T. Komino, M. Matsuda, S. Ikeda, Y. Ando, and H. Akiyama, Bull. Chem. Soc. Jpn. **79**, 549 (2006).

Authors

H. Tajima, K. Shimatani, T. Komino, M. Matsuda, S. Ikeda, Y. Ando, and H. Akiyama

---

Competition between "Superconducting" State and "Checkerboard-type Charge-ordered" State of New Organic Superconductors; β-(DMBEDT-TTF)$_2$X (X = PF$_6$, AsF$_6$)

Mori and Uwatoko Groups

So far, the organic superconductors, whose superconducting state is competitive with magnetic order like antiferromagnetic state or SDW state, have been intensively studied for κ-type ET salts and Bechgaard TMTSF salts. However, an organic superconductor, whose superconducting (SC) state is competing with a charge-ordered (CO) state is very rare [1]. Therefore, its superconducting mechanism has not been clarified experimentally yet, and only theoretical proposal submits the competitive superconducting symmetry between singlet and triplet states [2].

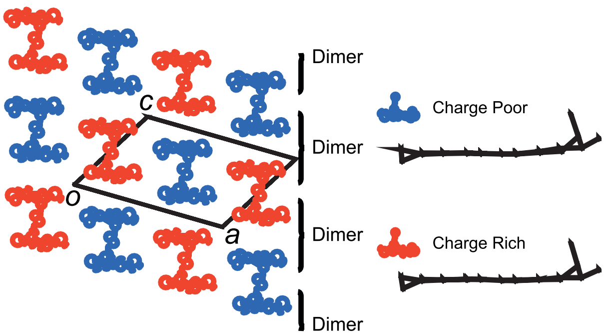

Fig. 1. Checkerboard-type charge-ordered state for β-(*meso*-DMBEDT-TTF)$_2$PF$_6$. The ~+0.7 charge rich (r; red) and the ~+0.3 charge poor (p; blue) molecules are arranged as a fashion of "rrpp" in the column.

On the way to apply the chemical negative pressure to ET salts by the introduction of the steric hindrance part to ET molecule, Mori group has discovered the new pressured-induced organic superconductors of β-(*meso*-DMBEDT-TTF)$_2$X (X = PF$_6$ [3] and AsF$_6$). At an ambient pressure, the metal-insulator (MI) transition occurs at 90 K for the PF$_6$ and AsF$_6$ salts. The magnetic susceptibility, however, follows the Heisenberg model with J = 105 K even in the metallic region without the anomaly at the MI transition at 90 K. In order to clarify the insulating state below 90 K, the crystal structure analysis by utilizing synchrotron X-ray radiation has been performed at 11.5 K. As a result, the checkerboard-type CO state was exhibited as shown in Fig.1 [4]. The ~+0.7 charge rich (r) and the ~+0.3 charge poor (p) molecules are arranged in the manner of "rrpp". This checkerboard-type CO pattern could not be explained only by the intermolecular Coulomb repulsion (V), but also by the electron-phonon interaction and molecular degrees of freedom.

By applying pressure to the CO state, the MI transition temperatures are lowered and the superconducting transitions were observed at the onset temperature of resistance drop T_c = 4.3 K under 4 kbar for the PF$_6$ salt and T_c = 4.3 K under 3.8 kbar for the AsF$_6$ salt. The characteristic features are the resistivity upturn observed just above the resistance drop from 1.9 to 9.0 kbar. By applying magnetic field under 3.8 kbar, the temperature of resistivity drop (T_c) is lowered and the resistivity upturn is extended to lower temperatures owing to the suppression of superconductivity. Moreover, the magnetic-field-induced insulating states emerged below 13 K, indicating not only that the SC state is competitive with the CO state, but also that the SC state is deeply related to the CO state as shown in Fig. 2. Under 10.5 to 15 kbar, the metallic behavior is observed down to 0.5 K and the temperature dependence follows T^n with an increase of n from 1.3 (9 kbar) to 1.7 (15 kbar). It implies that the electronic state changes from non Fermi liquid at the boundary between the superconducting and the metallic region to the Fermi liquid in the metallic region under high pressure. The elucidated electronic phase diagram as shown in Fig. 3 demonstrates that the CO state covers the SC state in the large pressurized region.

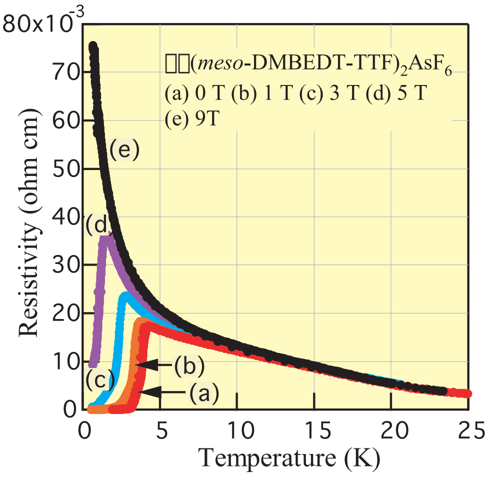

Fig. 2. Superconducting state and the magnetic-field-induced insulating state for β-(*meso*-DMBEDT-TTF)$_2$AsF$_6$.

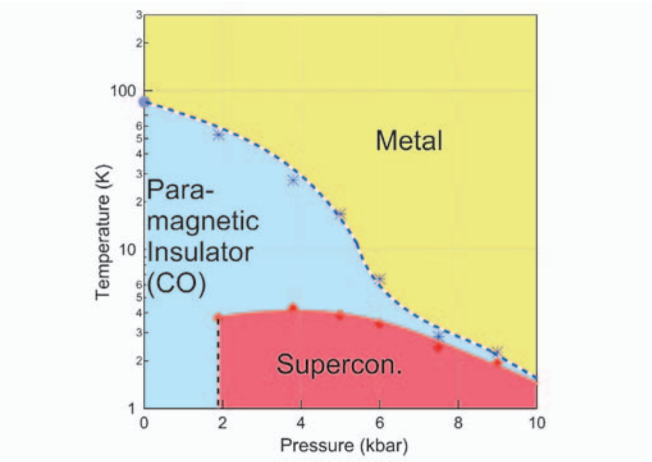

Fig. 3. Electronic phase diagram of β-(*meso*-DMBEDT-TTF)$_2$AsF$_6$, indicating the competition between superconducting and charge-ordered states.

These salts β-(*meso*-DMBEDT-TTF)$_2$X (X = PF$_6$ [3] and AsF$_6$) which show the superconductivity under the moderate pressure are suitable and promising materials to clarify the nature of CO suppressed superconductivity and the competition between SC and CO states.

References

[1] H. Mori, J. Phys. Soc. Jpn. **75**, 51003 (2006).
[2] Y. Tanaka, Y. Yanase, and M. Ogata, J. Phys. Soc. Jpn. **73**, 2053 (2004).
[3] S. Kimura, T. Maejima, H. Suzuki, R. Chiba, H. Mori, T. Kawamoto, T. Mori, H. Moriyama, Y. Nishio, and K. Kajita, Chem. Commun. 2454 (2004).
[4] S. Kimura, H. Suzuki, T. Maejima, H. Mori, J. Yamaura, T. Kakiuchi, H. Sawa, and H. Moriyama, J. Am. Chem. Soc. **128**, 1456 (2006).

Authors

H. Mori, S. Kimura, R. Chiba[a], H. Suzuki, J. Yamaura, M. Koeda, M. Hedo, Y. Uwatoko, T. Kawamoto[b], T. Mori[b], Y. Nishio[a], and K. Kajita[a]
[a]Toho University
[b]TIT

Control of the Spin State of a Light Atom by Changing the Density of Surrounding Conduction Electrons

Takada Group

Interests in spintronics are on the rise from both scientific and technological points of view. Since devices in spintronics involve active control and manipulation of spin degrees of freedom in solid-state systems, it is absolutely necessary to have a deeper understanding of fundamental interactions between electron spins and its solid-state environments. In view of this situation, we are interested in a composite system of an atom immersed into the otherwise homogeneous

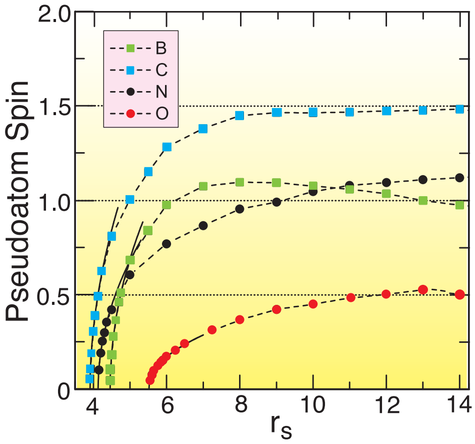

Fig. 1. Calculated total spin of the pseudoatom versus the EG density parameter r_s. Solid curves are the fittings of the data with the universal $(r_s$-$r_{sc})^{0.5}$ relation.

electron gas (EG).

In an isolated atom, the ground state obeys the Hund's multiplicity rule that requires the highest spin configuration compatible with the Pauli's exclusion principle. Physically this rule is interpreted as the consequence of an effectively larger nuclear charge in a higher spin configuration due essentially to the exchange effect.

Similarly in a uniform EG, the same effect favors spin polarization, bringing about the spontaneous spin-symmetry breaking or the spin-density-wave state which was proven to be the ground state at arbitrary electron densities within the Hartree-Fock (exchange only) approximation. The correlation effect, however, acts in the opposite direction and this effect is so strong in an EG as to lead eventually to the paramagnetic ground state for the majority of metals.

We have studied the ground state of the composite system (or pseudoatom) in the spin-density functional theory [1] and found several intriguing features such as (i) sharp transition from a spin-neutral state to a spin-polarized one with the decrease of the electron density of the EG, if the immersed atom is either B, C, N, or O; (ii) smooth evolution from the spin-polarized state of the pseudoatom to that of the negative ion of the corresponding isolated atom with the further decrease of the density; (iii) formation of the spherical combined spin density/charge density wave, which slowly decays with the distance from the immersed-atom site; and (iv) significant shrinkage of the size of the spin-polarized pseudoatom as compared with its spin-neutral counterpart.

In order to elaborate the first two points, we show the calculated total spin S of the ground-state pseudoatom as a function of r_s (the conventional parameter characterizing the electron density of the enveloping EG) in Fig. 1, which clearly indicates a spontaneous magnetization of the pseudoatom for r_s larger than some threshold value r_{sc}. The net electronic spin S depends on both r_s and the atomic number of the atom Z. This finds itself in contrast with the result for the net electronic charge around the atom, which is uniquely determined by Z due to the full screening of a charge in the EG.

The steep fall in S near the critical point in Fig.1 is suggestive of a "phase transition" of the second order. In fact, S is found to exhibit a universal behavior in accordance with "the mean-field theory" or in proportion to $(r_s$-$r_{sc})^{0.5}$ for r_s near r_{sc}.

Generally, the obtained S is not a multiple of 1/2. This fundamental difference between an isolated atom and this pseudoatom is brought about by the contribution of an infinite number of delocalized electrons in the latter, implying a complicated many-body nature in this atom-EG composite system.

The trend in S at low densities (large r_s) has a clear qualitative interpretation: Because of the positive electron affinity (EA) of the B, C, and O isolated atoms (0.010, 0.046, and 0.054 a.u., respectively), each atom immersed into the EG in the limit of zero density should be reduced into a negative ion (NI) of the corresponding atom. According to the Hund's rule, the population of the 2p orbitals is with 2 electrons with spin up (^{3}P), 3 electrons with spin up (^{4}S), and 3 electrons with spin up and 2 electrons with spin down (^{2}P) for B$^-$, C$^-$, and O$^-$ ions, respectively, corresponding to the total spin of 1, 3/2, and 1/2, respectively, which is clearly satisfied in Fig. 1 at large r_s. On the other hand, the NI of the N atom is unstable although long living (EA=-0.003 a.u.), and the slow growth of S of this pseudoatom between 1 and 3/2 at large r_s can be understood as the competition between the NI ^{3}P and atomic ^{4}S states.

Our model might be too primitive to discuss actual systems, but because of the sharpness of the transition in Fig. 1, we may suggest a novel method of spin manipulation by changing the carrier density in a system across the threshold. For example, we may think of an impurity atom in an appropriate semiconductor host, where the carrier density in the semiconductor will be altered by either applying the gate voltage in the FET (field-effect transistor) structure or optical pumping.

References

[1] V. U. Nazarov, C. S. Kim, and Y. Takada, Phys. Rev. B **72**, 233205 (2005).

Authors
V. U. Nazarov[a], C. S. Kim[a], and Y. Takada
[a]Chonnam National University

Ab Initio Simulation of Biased Surfaces/Interfaces

Sugino Group

Applying bias voltage is an effective means to modify surface properties as has been exemplified by recent scanning tunneling microscopy (STM) and electrochemical experiments. The bias of up to several eV can be applied to the region between the surface and the STM tip, typically less than 10 Å thick, inducing large electric field and surface charges. Even larger field and charge are induced when the surface is faced with the water solution because of the electric double layer effect. By precisely measuring the

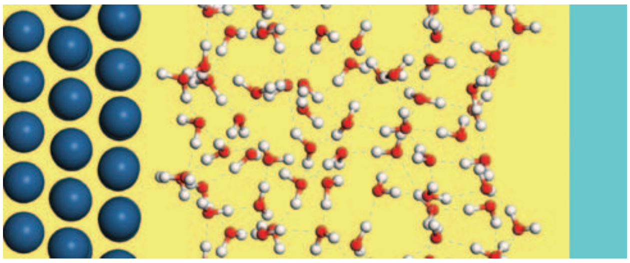

Fig. 1. A snap shot of the first-principles molecular dynamics simulation for the biased platinum-water interface done at the room temperature. The effective screening medium (ESM) with infinite ε is placed in the region painted with blue. Surface charge of about 1/150 [C/surface atom] is induced because of the applied bias.

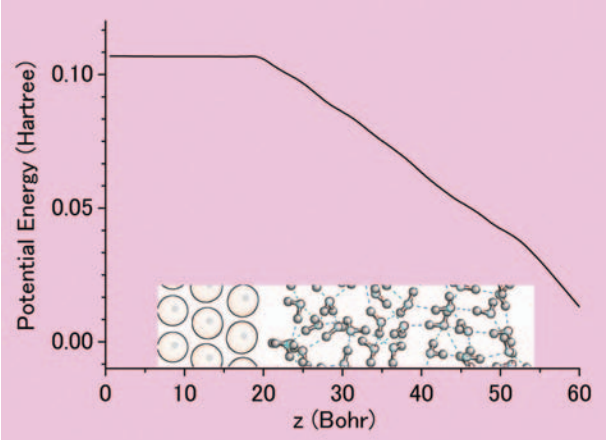

Fig. 2. Potential energy averaged over the surface parallel directions.

electronic and geometric response to this extreme condition, much experimental effort has been made to reveal undiscovered properties of the surface.

Introducing bias voltage to the first-principles simulation is a rather difficult problem because the simulation techniques for the surfaces have been developed mainly assuming the periodic boundary condition (PBC), which is incompatible with the biased surfaces. The induced charge is also incompatible because the electrostatic energy diverges unless the screening effect of the STM tip or the water solution is properly taken into account. To overcome these problems without increasing computational demand of the simulation, we developed a new approach to the biased surfaces/interfaces, called effective screening medium (ESM).

In this approach, the system is represented by the surface slab model that is in contact with a continuum represented by the local permittivity, ε, and by the distribution of classical ions in the solution, *i.e.*, the electrolyte ions. For example, the STM tip is modeled by using infinite ε and the water solution is modeled by using ε=78.4 and the Poisson-Boltzmann (PB) distribution of the classical ions. Importantly, owing to the screening effect of the continuum, charged surface can be handled without the electrostatic energy divergence, and also, the vacuum level can be unambiguously determined to define the bias voltage in accordance with the experimental conditions.

The total-energy functional is then

$$K\left[\rho_e\right] + E_{xc}\left[\rho_e\right] - \int d\mathbf{r}\frac{\varepsilon(\mathbf{r})}{8\pi}\left|\nabla V(\mathbf{r})\right|^2 + \int d\mathbf{r}\,\rho_{tot}(\mathbf{r})\,V(\mathbf{r}),$$

where the first two terms are kinetic and exchange-correlation energy for the electrons and the last two terms are electrostatic energy for the electrons, nuclei, and electrolyte ions (ions in the water solution). This is different from the conventional total-energy functional in that the local permittivity ε appears here to represent the effective screening medium (ESM). Importantly, the equations derived from the total-energy functional, *i.e.*, the Poisson and the Kohn-Sham equations, usually have a structure in our target systems which can be solved without introducing the periodic boundary condition (PBC) in the surface normal direction. In this case, contrary to the conventional scheme, Green's function technique needs to be introduced for the Poisson equation but the computational demand required additionally is almost negligible.

The effective screening medium (ESM) approach thus enables us to handle surfaces even when biased and charged up, when the counter electrodes, *e.g.*, the STM tip or the water solution, can be modeled by the continuum. We have successfully applied the ESM to organic molecules on the silicon surface, carbon nanotubes on the backgate, and the platinum-water interfaces with help of collaborators. Figure 1 is a snapshot for the first-principles molecular dynamics simulation for the biased platinum-water interface. The Pt surface layers and water molecules are represented within the generalized gradient approximation (GGA) for the density-functional theory (DFT) and the effective screening medium (ESM) with infinite ε is placed beyond the water. The potential profile, shown in Fig. 2, shows that the potential gradient has a finite and almost constant value because of the dielectric screening of the water but is zero in the substrate because of induced surface charge and strong metallic screening of the platinum. With intensive use of the ISSP supercomputers and the Earth Simulator (ES), the simulation is now performed to elucidate the electrolysis of water, which is the most fundamental electrochemical reaction and the microscopic detail has been unknown yet.

References

[1] M. Otani and O. Sugino, Phys. Rev. B **73**, 115407 (2006).

Authors

M. Otani, Y. Yoshimoto, and O. Sugino

Resistively-Detected NMR in Quantum Hall Systems

Iye and Katsumoto Groups

Quantum Hall (QH) systems, *i.e.*, two-dimensional (2D) carrier systems in semiconductor heterostructures under the condition of high magnetic field and low temperature, exhibit a wide variety of many body ground states depending on the Landau level (LL) filling factor ν, including integer and fractional quantum Hall liquids, Wigner solids, stripe and bubble phases, and composite fermion liquids. In recent years, phenomena associated with the spin degree of freedom have attracted much attention. They include, spin phase

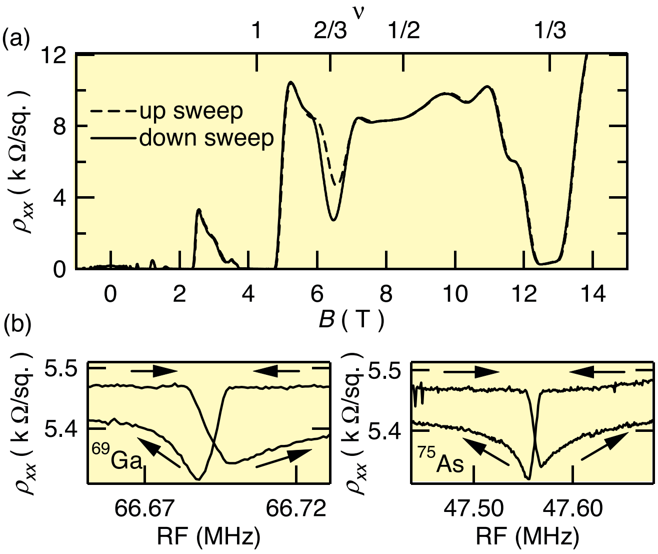

Fig. 1. (a) Magnetoresistance of high mobility 2DEG sample showing hysteretic behavior at around ν=2/3 associated with the spin transition of the quantum Hall system. Resistively detected nuclear magnetic resonance signals for the ^{69}Ga and and ^{75}As nuclei at ν=2/3 are shown in (b) and (c).

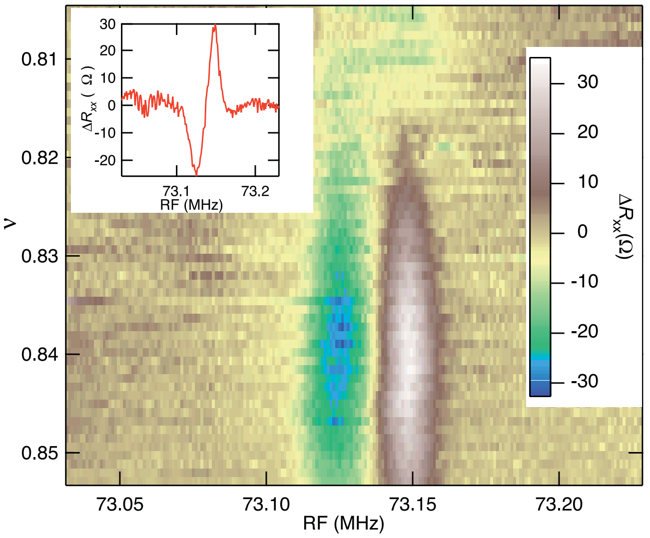

Fig. 2. The inset shows an anomalous “dispersive” lineshape of RDNMR in the vicinity of $\nu=1$. The main panel is a color-scale plot showing the evolution of the anomalous RDNMR lineshape as a function of ν.

transition of fractional quantum Hall states, spin polarization of composite fermions, skyrmion excitations in quantum Hall ferromagnets, and interaction between electron and nuclear spins. A dramatic effect involving nuclear spins has been observed in 2D electron system (2DES) at $\nu=2/3$, where the effect manifests itself as a hysteretic behavior of magnetoresistance with a very long relaxation time scale[1]. The ground state can be spin-polarized or spin-unpolarized depending on the magnetic field range where this state occurs. When the two spin states are nearly degenerate, domains of different spin polarization states may be formed. When the energy difference between the different electron spin states is comparable to the nuclear Zeeman energy, the electron-nuclear spin flip process via hyperfine coupling is energetically allowed.

Figure 1-(a) shows the magnetoresistance trace of a high mobility 2DEG sample, which shows hysteretic behavior at $\nu=2/3$, when it occurs at relatively low magnetic fields (B<8T). Shown in Figs. 1-(b) and (c) are the resistively detected nuclear magnetic resonance (RDNMR) signals the ^{69}Ga and ^{75}As nuclei in this regime.

With appropriate tuning, RDNMR signals can be detected over a rather wide range of filling factors[2], though the signal intensity varies significantly. Another QH regime where RDNMR signal can be conspicuously detected is the vicinity of $\nu=1$ where skyrmions (spin textures) constitute low-lying excitations. In this regime, anomalous “dispersive” RDNMR lineshape, whose origin is not completely understood, is observed. The dispersive lineshape is found to evolve into an ordinary one as we move further away from $\nu=1$. The temperature dependence of the nuclear spin-lattice relaxation rate $1/T_1$ in the latter regime is found to be Korringa-like, while that in the range of ν where anomalous lineshape is observed is larger in magnitude and increases with decreasing temperature. The implication of these anomalous behaviors for the skyrmion physics is currently explored.

References

[1] S. Kronmueller *et al*., Phys. Rev. Lett. **81**, 2526 (1998); *ibid*. **82**, 4070 (1999).
[2] K. Hashimoto et al. Phys. Rev. Lett. **88**, 176601 (2002); W. Desrat *et al*., Phys. Rev. Lett. **88**, 256807 (2002).

Authors
K. Kodera, H. Takado, A. Endo, Y. Hashimoto, S. Katsumoto, and Y. Iye

Quantum Dot with Zero Electron Still Causes the Fano Effect

Katsumoto Group

A quantum dot (QD) is often defined as a "droplet" of electrons. Here we would like to show, however, that a potential dip with no electron also works as a QD in interference circuits. A quantum wire with a side-coupled QD is a simplest circuit to cause quantum interference, that is, the interference between the direct path through the wire and the path with reflection to the dot. Because squeezing of the dot by surrounding depletion layer pushes it to the wire, the number of electrons can be reduced to zero without reducing the coupling strength between them. This feature enables us to explore the interference effect around resonance points, *i.e.*, the Fano effect in QDs with few electrons [1].

The inset of Fig.1 shows a micrograph of the sample. We measured the conductance of the wire as a function of the gate voltage $V_{\rm w}$, which suppresses the width of the wire and the gate voltage $V_{\rm g}$, which controls both the dot size and the electrostatic potential of the dot. As is well known, the conductance of the wire is approximately quantized versus $V_{\rm g}$ and the interference effect appears as small deviation from such stepwise variation. Figure 1 displays the variation of wire conductance from the stepwise baseline in a colored plot as a function of $V_{\rm w}$ and $V_{\rm g}$.

In the transition regions between the conductance steps, the response to $V_{\rm g}$ is a mixture of the interference effect and the effect of changes in the electrostatic potential and inevitably has large amplitudes. The regions with small amplitudes indicated by Q_m's are on the quantized plateaus and pure interference effect is observed. There vertically elongated blue-red stripes are observed, which indicate the

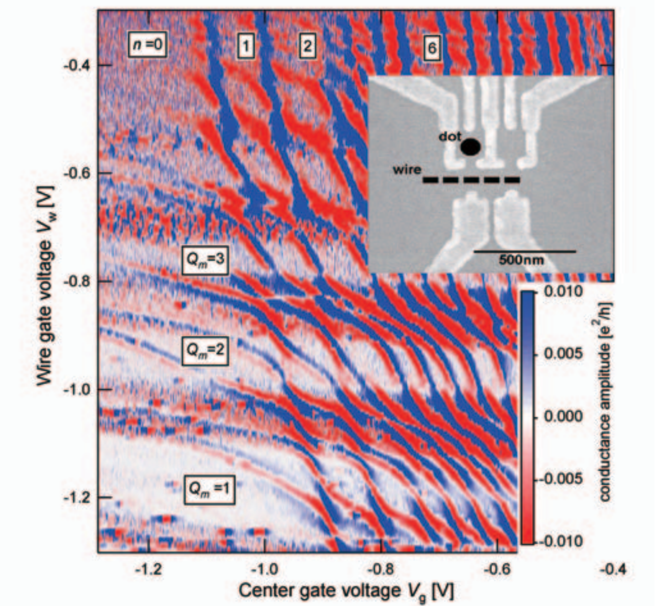

Fig. 1. Color plot of variation in conductance of a quantum wire with a side-coupled quantum dot. Quantized stepwise conductance variation is subtracted as the baseline. $Q_{\rm m}$ is the height of "base" conductance step and n is the number of electrons in the dot counted by starting at n =0 region.

Fano effect around the Coulomb peaks of the dot. The distances between them in V_g axis thus reflect the "addition energy" of an electron to the dot.

We see no such vertical structure in the region captioned as "n=0", where no electron exists in the dot. This is supported by several facts, *e.g.*, disappearance of strong signal in the plateau-plateau transition regions. Now we can count the number of the electrons in the dot starting from the zero-electron state and then find that the spacing between the Coulomb peaks is apparently wider at "n=2" and "n=6". They correspond to closed shells of a two-dimensional isotropic harmonic potential, that is, $N(N+1)$ (N=1,2). This means the electrons are confined with a comparatively circular potential.

Then why we still see blue-red structures (not vertical but slanted to V_g axis) in the region n=0? Part of electron wavefunction goes even into the empty dot and causes some resonance and interference. Hence an empty QD can cause the Fano effect.

References

[1] K. Kobayashi, H. Aikawa, S. Katsumoto, and Y. Iye, Phys. Rev. Lett. **88**, 256806 (2002).

Authors
T. Otsuka, Y. Iye, and S. Katsumoto

Switching Magnetization of Nano-Scale Ferromagnetic Particle by Non-Local Spin Injection

Otani Group

Spin-dependent transport properties in ferromagnetic/nonmagnetic hybrid structures have drawn much attention owing to the novel idea to utilize the spin angular momentum for future spintronic devices. Instead of the conventional inductive recording method, the spin angular momentum transfer of conduction electrons is now employed to switch the magnetization. The switching mechanism due to the spin transfer can be understood by considering the spin torque which is proportional to the injected spin current. So far, most of the current studies related to the spin torque are performed using vertical multilayered nanopillars in which two magnetic layers are separated by a nonmagnetic metal layer. In such structures, the charge current always flows together with the spin current, thereby undesirable Joule heat and Oersted field are generated.

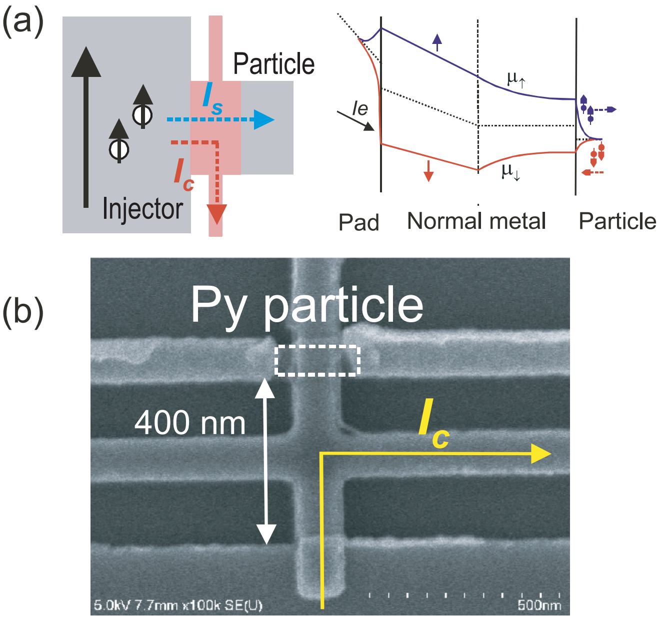

Fig. 1. (a) Schematic illustration of the non-local spin injection using lateral spin-valve geometry. Only spin current is injected into the small ferromagnetic particle. (b) Scanning electron microscope image of the fabricated lateral spin valve. The device consists of a large Py injector 30 nm in thickness, a Cu cross 100 nm in width and 80 nm in thickness, and a Py nano-scale particle, 50 nm in width, 180 nm in length and 6 nm in thickness.

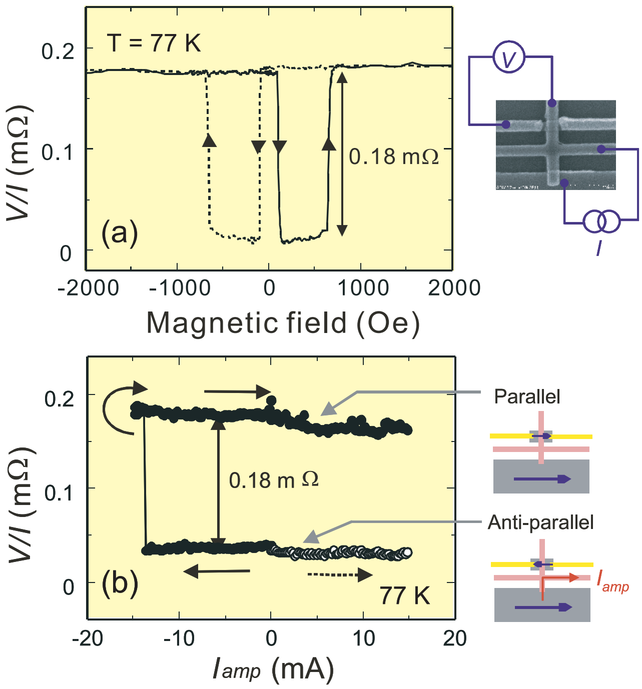

Fig. 2. (a) Field dependence of the non-local spin signal. The resistance changes at low and high fields correspond to the relative magnetic switching of the Py injector and particle, from parallel to anti-parallel states and *vice versa*. (b) Non-local spin valve signal after the pulsed current injection as a function of the current amplitude with corresponding magnetization configurations.

Our recent experiments revealed that the spin currents induced by the non-local spin injection are effectively absorbed into an additionally connected ferromagnet because of the short spin diffusion length. There is therefore a high possibility that the spin current without a charge flow is selectively injected into a ferromagnetic small particle and switch the magnetization of the small ferromagnetic particle. To test this idea, we fabricated a lateral spin valve including a nano-scale Permalloy (Py) particle as shown in Figs. 1 (a) and (b).

To confirm that the spin current from the Py injector is injected into the Py particle, the non-local spin valve measurements are performed. As in Fig. 2 (a), the field dependence shows a clear spin-valve signal with the magnitude of 0.18 mΩ, assuring that the spin current reaches the Py particle.

Then, we examine the effect of the non-local spin injection into the Py particle with using the same probe configuration. Before performing the non-local spin injection, the magnetization configuration is set in the anti-parallel configuration by controlling the external magnetic field. The non-local spin injection is performed by applying large pulsed currents up to 15 mA in the absence of magnetic field. As shown in Fig. 2(b), when the magnitude of the pulsed current is increased positively in the anti-parallel state, no signal change is observed up to 15 mA. On the other hand, for the negative scan, the abrupt signal change is observed at -14 mA. The change in resistance at -14 mA is 0.18 mΩ, corresponding to that of the transition from anti-parallel to parallel states. This means that the magnetization of the Py particle is switched only by the spin current induced by the non-local spin injection. The responsible spin current for switching is estimated from the experiment to be about 200μA, which is reasonable compared with the values obtained for conventional pillar structures.

References
[1] T. Kimura, Y. Otani, and J. Hamrle, Phys. Rev. B **72**, 014461 (2005).
[2] T. Kimura, Y. Otani, and J. Hamrle, Phys. Rev. Lett. **96**, 037201 (2006).

Authors
T. Kimura and Y. Otani

Remote Atomic Manipulation of Dimer Buckling through Carrier Propagation in the Surface States

Komori Group

Electronic excitation induced by tunneling electrons in scanning tunneling microscopy (STM) often moves the atoms under the tip. On the clean Ge(001) surface, it locally inverts the buckling orientation of the Ge dimers without cutting the Ge bond below 80 K [1]. Moreover, we can reversibly control the orientation to change the area of local c(4×2) or p(2×2) structures by selecting the sample bias voltage V_b in the STM operation. The two different local structures coexist on the same surface when V_b is between - 0.6 V and 0.7 V. In the other range of V_b, one of the two structures covers the whole surface when it is scanned by the STM tip. The mechanism of the transformation is explained by a coherent climbing of the vibrational state of the dimer by electronic excitation [2].

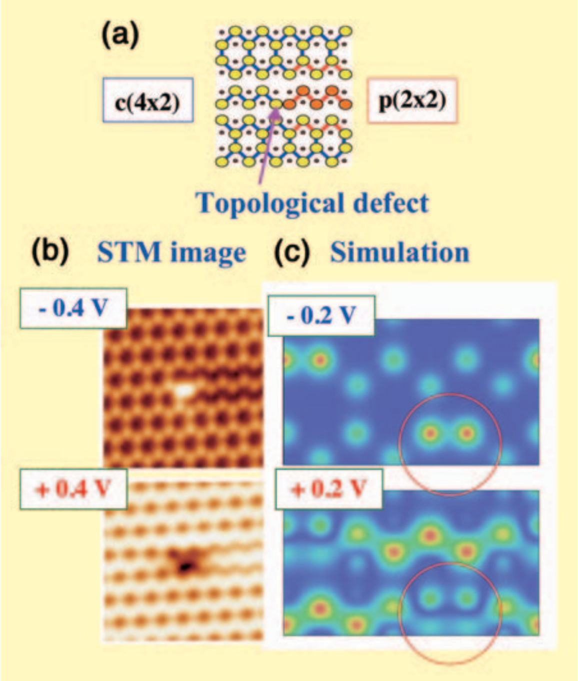

Fig. 1. (a) Schematic model of the topological defect between c(4×2) and p(2×2) areas on the Ge(001) clean surface. (b) STM images of the defect for two sample bias voltages. The image area is 6 nm × 6 nm. (c) Simulated STM images including the defect(red circle) on the basis of the first-principles calculation.

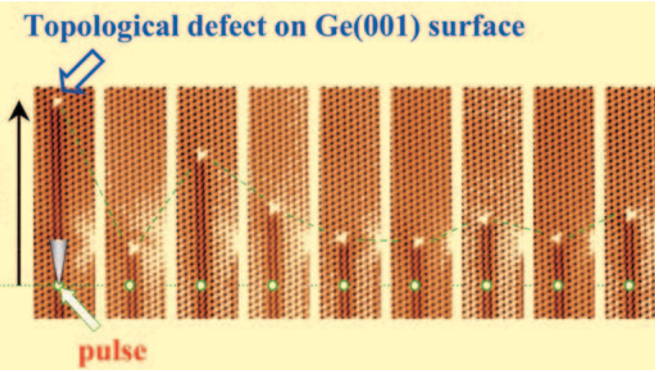

Fig. 2. STM images showing one-dimensional motion of the topological defect on the Ge(001) surface by pulse current injection. Each time after the injection of electrons from the STM tip at the point of the green circle, the defect moves in the dimer-row direction. The center of its random walk is 8 nm apart from the point of the electron injection by the bias voltage pulse to 0.8 V. The center position separates further with increasing the bias voltage during the electron injection. When we decrease the bias voltage below 0.7 V, the defect comes just under the STM tip.

The electron tunneling from or to the STM tip remotely creates and moves a metastable topological defect between c(4×2) and p(2×2) shown in Fig. 1. Hot electrons or holes created in the Ge surface states by the tunneling propagate along the surface, and induce the defect motion in the dimer row direction through the electron-lattice interaction, as demonstrated in Fig. 2. The direction of its motion depends on the electric field due to STM bias through the electric dipole of the Ge dimer. We have measured the rate of the defect motion induced by tunneling electrons as a function of the distance and the direction between the defect and the tunneling point, and the bias voltage during the pulse. The threshold distance of the motion rapidly increases with increasing the absolute value of the bias voltage for the both polarities. It is much longer in the dimer row direction than in the dimer direction for the transformation by electron injection. On the other hand, the distance is almost isotropic for the transformation by hole injection. The difference is attributed to that in the lifetime of the excited carriers in the surface electronic states on the basis of the band calculation [3].

References
[1] Y. Takagi, Y. Yoshimoto, K. Nakatsuji, and F. Komori, J. Phys. Soc. Jpn. **72**, 2425 (2003).
[2] H. Kawai and O. Narikiyo, J. Phys. Soc. Jpn. **73**, 2362 (2004) .
[3] K. Nakatsuji, Y. Takagi, F. Komori, H. Kusuhara, and A. Ishii, Phys. Rev. B **72**, 241308(R) (2005).

Authors
Y. Takagi, K. Nakatsuji, Y. Yoshimoto, and F. Komori

A Compact UHV System for Fabrication and *in situ* Analysis of Electron Beam Deposited Structures using a Focused Low Energy Electron Beam

Yoshinobu Group

A UHV system has been developed in order to fabricate and *in situ* analyze micro- and nanostructures. The system includes a low energy electron gun which provides a minimum spot size of ~25 nm in a diameter using electrostatic lenses, a cylindrical mirror analyzer for Auger electron spectroscopy

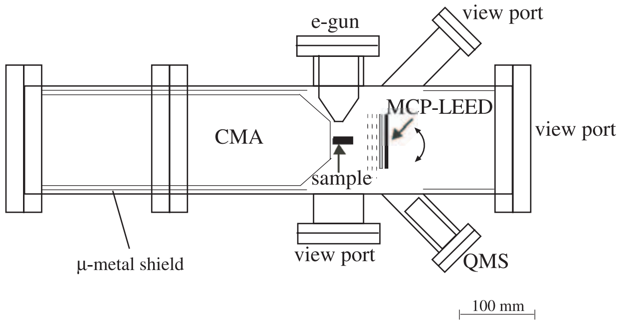

Fig. 1. Top view of the present UHV system including a focused electron beam source, a CMA, a QMS, an MCP-LEED and a μ-metal shield.

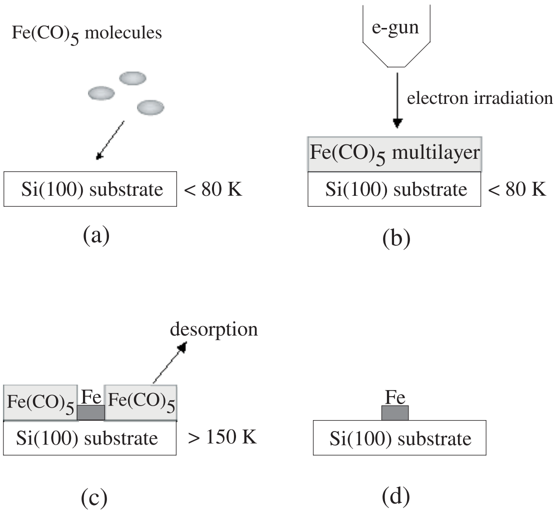

Fig. 2. The process diagram of electron-induced deposition of $Fe(CO)_5$. (a) $Fe(CO)_5$ molecules are physisorbed on the Si(100) surface below 80 K. (b) The $Fe(CO)_5$ multilayer is irradiated by an electron beam area-selectively. (c) Intact $Fe(CO)_5$ molecules are desorbed by heating up to 150 K. (d) An iron artificial structure is formed at the electron beam irradiated position.

(AES) and electron energy loss spectroscopy (EELS), a low energy electron diffraction (LEED) instrument, and a scintillation counter for scanning electron microscopy (SEM) as schematically shown in Fig. 1 [1]. Using the electron gun, we can analyze electronic states of microscopic structure. In addition, we also fabricate submicron structures artificially by means of scanning a focused low-energy electron beam.

In order to demonstrate the performance, we fabricated an iron microstructure by electron beam induced deposition of iron pentacarbonyl ($Fe(CO)_5$), which was characterized by *in situ* AES, EELS and LEED analysis. The details of the process are as follows: (a) an Si(100) clean surface is prepared; (b) gaseous $Fe(CO)_5$ molecules are deposited on the Si(100) clean surface at 80 K; (c) the $Fe(CO)_5$ multilayer on the Si(100) clean surface is irradiated by a focused electron beam by controlling the beam position and scanning speed; (d) the Si substrate is heated to 150 K in order to desorb intact $Fe(CO)_5$ molecules which have not been irradiated by an electron beam. The diagram of this process is summarized in Fig. 2.

Figure 3 shows AES spectra of Fe $M_{2,3}VV$ and $SiL_{2,3}VV$ for (a) clean surface (b) after electron-induced deposition of $Fe(CO)_5$, at the position of electron beam irradiation (c) at the position of non-irradiation. These spectra were taken after desorption of the remaining intact $Fe(CO)_5$ by heating. At the electron-irradiated position, the Si $L_{2,3}VV$ peak at 92 eV is decreased in intensity, and an Fe $M_{2,3}VV$ peak appears at 47 eV (Fig. 3(b)). On the other hand, at the non-irradiated position, only an Si $L_{2,3}VV$ peak is observed after the desorption of intact $Fe(CO)_5$ (Fig. 3(c)). Thus, the Fe exists only at the electron beam irradiated position. In addition, the newly formed structure is metallic Fe judging from the Auger peak position. Note that metallic Fe and $Fe(CO)_5$ can be clearly distinguished in their energies; the Auger peak is observed at 37 eV for the $Fe(CO)_5$ molecules and at 47 eV for metallic Fe, respectively.

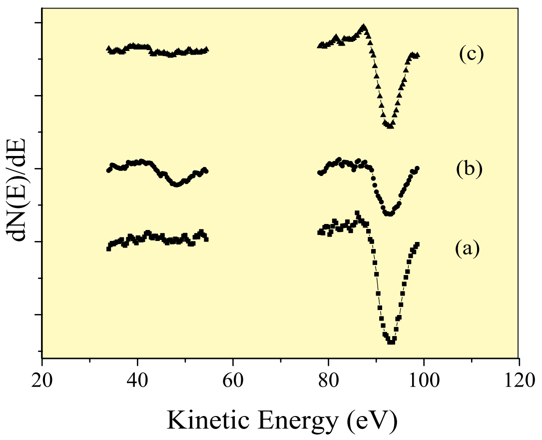

Fig. 3. AES spectra of the Fe $M_{2,3}VV$ and $SiL_{2,3}VV$ regions for (a) clean surface (b) after electron-induced deposition of $Fe(CO)_5$, at the position of electron beam irradiation (c) at the position of non-irradiation. The temperature of the Si(100) substrate was 80 K.

Figure 4 shows an example of a fabricated submicron iron structure. The size (including film thickness) and the position of microstructures are controllable with deposited molecules and electron beam irradiation. The present low energy electron beam system with electrostatic lenses is very useful for electron spectroscopy of artificial microstructures on surfaces.

References

[1] Y. Kakefuda, Y. Yamashita, K. Mukai, and J. Yoshinobu, Rev. Sci. Inst. **77**, 053702 (2006).

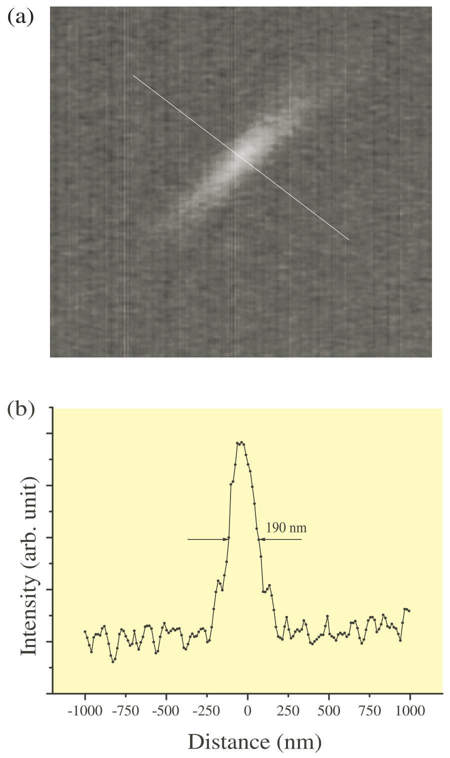

Fig. 4. (a) An SEM image after Fe deposition by an electron beam irradiation at 80 K followed by heating to 150 K. The area of this image is 3×3 μm^2. The total dose of electrons is 2×10^{-14} C on the $Fe(CO)_5$ multilayer (600 L). (b) An SEM line profile. The full width at half maximum of this iron structure is 190 nm.

Authors
Y. Kakefuda, Y. Yamashita, K. Mukai, and J. Yoshinobu

Real-Space Observation of Screened Potential by Scanning Tunneling Spectroscopy

Hasegawa Group

The electrostatic potential around a single charge in vacuum is described with the Coulomb potential. If the charge is situated in a metallic electron system, the Coulomb potential is modified by electrons in the system. The modification of the potential, called screening, is one of the fundamental phenomena in the condensed matter physics. Using scanning tunneling microscopy / spectroscopy (STM/S) we developed a method for measuring electrostatic potential in high spatial and energy resolutions, and performed a real-space observation of the potential around external charges screened by two-dimensional surface electron gas (2DEG). In the real-space potential mapping, characteristic decay and oscillation in the potential, so-called, the Friedel oscillation, were clearly visible around the charges [1].

As a sample having a two-dimensional surface electron system, we used the Si(111)-$\sqrt{3}\times\sqrt{3}$-Ag surface. The electron standing wave patterns [2] are observed in tunneling conductance (dI/dV) images and an energy dispersion curve obtained from the images exhibits an isotropic and parabolic shape, indicative of free-electron like behaviors of the electrons in the states. It has been known that when the surface potential is changed, for instance, by additional Ag adsorption on the surface, an energy level of the surface states also shifts accordingly. Therefore, by measuring the energy level of the surface states locally by using STS, one can obtain a mapping of the potential on the surface.

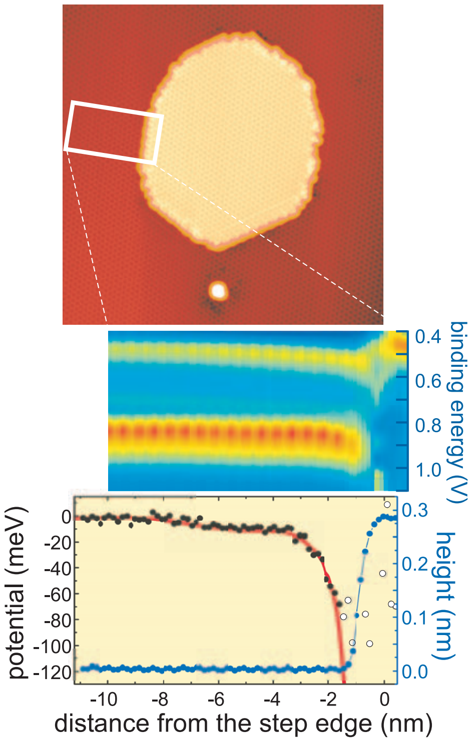

Fig. 1. (upper): an STM image (40×40nm^2) on the Si(111)-$\sqrt{3}\times\sqrt{3}$-Ag surface. (middle): A series of tunneling spectra taken in the rectangular area are shown in a color-coded manner. The -0.85eV peak shifts to higher binding energy as approaching to the step edge. (bottom): the peak energy shift as a function of distance from the step edge. It can be fitted well by the screened potential.

The obtained potential profiles around Ag adsorbates and step edges, where the Ag adsorbates are accumulated, were fitted well with theoretically predicted potential profiles, as shown in Fig. 1. In the area marked with a rectangle on the STM image of Fig. 1, the tunneling spectra were measured from the terrace to the step edge, and the obtained spectra are plotted in a color-coded manner in the middle of Fig. 1. In the spectra a peak around -0.85eV is due to one of the electronic states of the surface, called S_2/S_3 states. The binding energy of the S_2/S_3 state is found to shift to the higher binding energy as the measured position approaches to the step edge. The amount of the shift as a function of a distance from the step edge is plotted in the lower panel of Fig. 1. This is the electrostatic potential profile around the step edge of the surface, we thought.

In order to confirm our speculation, we calculated an expected potential profile on the surface. Assuming the step edge has positive charges, which is due to the adsorbed Ag adatoms on the step edge, the potential around the step edge should behave like a Coulomb potential. Since the surface has 2DEG, the Coulomb potential is modified or "screened" by the 2DEG electrons. The screened potential can be calculated from a dielectric function of 2DEG, which was derived from the Lindhard theory. The calculated screened potential is fitted to the observed profile in the lower panel of Fig. 1, showing good agreements.

A wiggling feature in the screened potential is observed in the figure and called Friedel oscillation. The oscillation should have a period of the half Fermi wavelength of the 2DEG since it arises from a sharp cutoff in the 2DEG dielectric function at the corresponding wave number. From careful comparison, we found that the oscillation period is same as that of the electron standing wave at the Fermi energy, which is also a half Fermi wavelength. These results confirm that the observation of the screened potential and the Friedel oscillation from the STS.

References
[1] M. Ono, Y. Nishigata, T. Nishio, T. Eguchi, and Y. Hasegawa, Phys. Rev. Lett. **96**, 016801 (2006).
[2] Y. Hasegawa and Ph. Avouris, Phys. Rev. Lett. **71**, 1071 (1993)

Authors
M. Ono, Y. Nishigata, T. Nishio, T. Eguchi, and Y. Hasegawa

Insulator-Metal-Superconductor Transitions Induced by Electric Field Effect

Lippmaa Group

The physical properties of many oxides depend in a sensitive way on the concentration of charge carriers. The phase diagrams of cuprate superconductors and colossal magnetoresistance manganites have been studied in particular detail. Our work is aimed at controlling the carrier density in thin oxide films by field effect, rather than by chemical doping. Field-effect devices can be used to induce sufficient effective doping levels in thin layers to cause phase changes, such as metal-insulator or normal-superconducting transitions. Some of the device structures that we are using are shown in Fig. 1. The biggest challenge is to grow very thin epitaxial layers and heterointerfaces of oxides with sufficient quality for observing doping-related phase changes. So far, we have focused on structures based on undoped $SrTiO_3$ and Nb-doped $SrTiO_3$.

An oxide field-effect transistor (FET) is illustrated in Fig. 1(a). A $SrTiO_3$ substrate was used as the active channel material and a wide-gap insulator, $CaHfO_3$, was used as a gate insulator. The channel-insulator interface was grown epitaxially to reduce trapping [1]. $SrTiO_3$ is suitable for observing phase changes caused by field-effect doping, because the normally insulating material can become metallic and even superconducting at very low carrier densities of about 10^{20} cm^{-3}. Indeed, by applying a gate bias to a $SrTiO_3$ FET, we can observe an increase of channel current with reducing temperature, as shown in Fig. 2(a). The transition into a metallic state occurs at a gate bias of 1.3 V. Below this bias, the device is in an insulating state, with the channel current dropping at lower temperatures.

A different route to field-effect doping is illustrated in Fig. 1(b). In this case the gate electrode is replaced with a ferroelectric thin film $Pb(Zr,Ti)O_3$, which can be poled locally with the conducting tip of an atomic-force microscope (AFM) [2]. By choosing the polarity of the poling voltage, it is possible to either accumulate or deplete carriers in the thin Nb-doped $SrTiO_3$ layer. Doped $SrTiO_3$ becomes superconducting below about 300 mK. The transition temperature is a function of the number of carriers, which we modulate by poling the ferroelectric cover layer. The device is patterned as a usual Hall bar, allowing various transport measurements to be made. Only the region shown in red in Fig. 1(b) is poled by AFM.

The effect of poling the $Pb(Zr,Ti)O_3$ layer in opposite directions on the superconducting transition temperature of a thin Nb:$SrTiO_3$ layer can be seen in the bottom panel of Fig. 2. A clear shift to higher temperature can be seen in the P- state, which corresponds to an increase of carrier density. If the temperature is fixed at about 260 mK, local switching of superconductivity is possible.

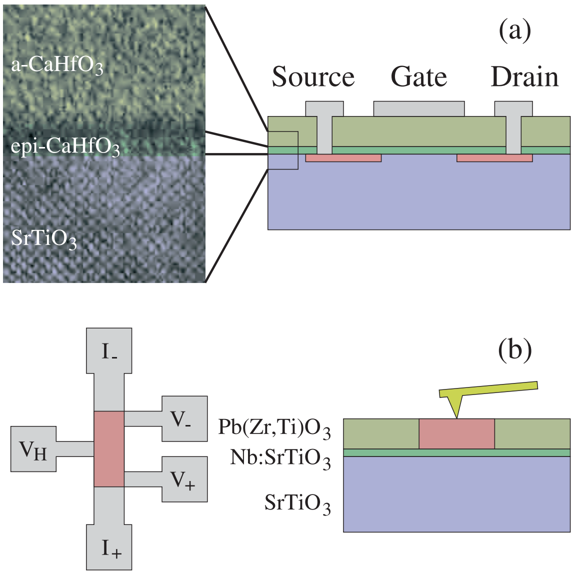

Fig. 1. (a) The device structure of an epitaxial oxide FET. A transmission electron microscope image shows details of the channel interface. (b) A device where the carrier density in a thin superconducting Nb-doped $SrTiO_3$ layer is modulated by changing the poling direction of a ferroelectric $Pb(Zr,Ti)O_3$ cover layer.

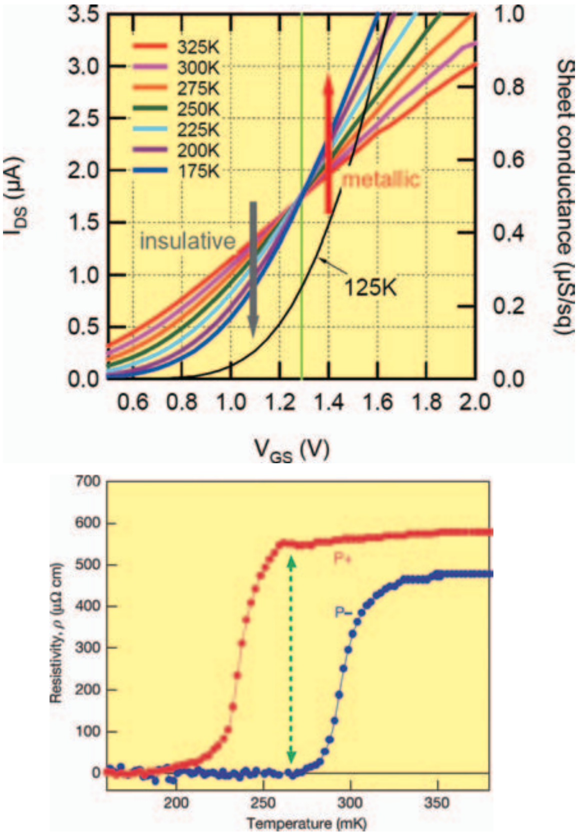

Fig. 2. (Top) The channel current of a $SrTiO_3$ FET as a function of gate bias and temperature. The channel becomes metallic above a gate bias of 1.3 V. (Bottom) The shift of the superconducting transition temperature of a Nb:$SrTiO_3$ layer, caused by accumulating (P- state) or depleting (P+ state) carriers from the film.

References

[1] K. Shibuya, T. Ohnishi, T. Uozumi, T. Sato, M. Lippmaa, M. Kawasaki, K. Nakajima, T. Chikyow, and H. Koinuma, Appl. Phys. Lett. **88**, 212116 (2006).

[2] K. S. Takahashi, M. Gabay, D. Jaccard, K. Shibuya, T. Ohnishi, M. Lippmaa, and J.-M. Triscone, Nature **441**, 195 (2006).

Authors

M. Lippmaa, K. Shibuya, T. Ohnishi, K. S. Takahashi[a], and J.-M. Triscone[a]
[a]University of Geneva, Switzerland

Magnetization Measurements of Two Dimensional Solid ^3He on a Layer ^4He Pre-Plated Graphite

Ishimoto Group

^3He film adsorbed on graphite surface is one of the most ideal two-dimensional (2D) Fermi system which can realize not only a Fermi liquid but also a quantum solid with a triangular lattice only by changing the adsorption density. The transition between them is recently considered to be a sort of Mott transition [1]. The solid forms a quantum spin magnet with nuclear spin $S = 1/2$ on a triangular lattice. Because of the hard-core potential between ^3He atoms, the higher order multiple spin exchange (MSE) processes as well as two-particle exchange play important roles. The exchange of even number of particles is anti-ferromagnetic (AFM), while that of an odd ones is ferromagnetic (FM). The competition between them, in addition to the geometrical frustration inherent to a triangular lattice structure, makes the solid ^3He film strongly frustrated.

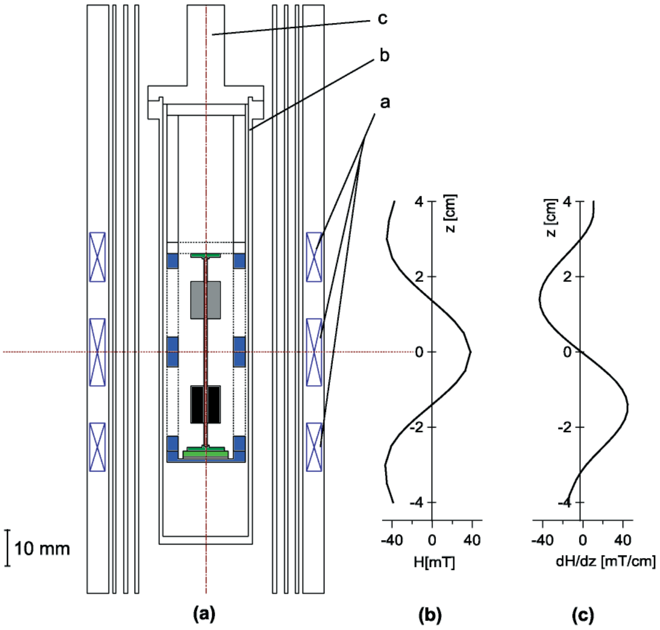

Fig. 1. Schematic drawing of double gradient coil Faraday-type magnetometer.

Recent theoretical studies in the exact diagonalization method for this finite size system show that none of long range ordered AFM phases survive even at T = 0 K due to quantum fluctuations. The exchange parameters so far obtained in the AFM region (so called 4/7 phase) predicts a quantum spin liquid (QSL) ground state with a finite excitation gap [2], and a magnetization plateau at around 5 to 6 T. Nevertheless the heat capacity and susceptibility measurements seem to indicate a gapless spin liquid ground state [3,4]. To solve this discrepancy, the magnetization curve in high magnetic fields has been tried.

A Faraday-type magnetometer has been developed to measure small nuclear magnetization of monolayer ^{3}He films adsorbed on Grafoil at temperatures well below 1 mK in high magnetic fields up to 10 T. The magnetic force is measured capacitively by monitoring the displacement of a wire-suspended copper plate, on which are diffusion-bonded many copper foils interleaved by Grafoils. To eliminate a large background signal from Grafoil and copper, a double gradient coil system is employed to produce opposite field gradients in two regions equidistant from the field center. The upper region contains Grafoil and the lower region contains non-exfoliated graphite sheets as shown in Fig.1.

The paramagnetic first layer and ferromagnetic second layer show the expected magnetization curve, proving that most of the background signal is well cancelled out. While the results of AFM 4/7 phase on both ^{3}He and ^{4}He mono layer pre-plated graphite show no saturated magnetization even at 1 mK and 10 T, suggesting the existence of magnetization plateau. Further development to clarify the whole magnetization behavior is now under way.

References
[1] A. Casey, H. Patel, J. Ny'ki, B. P. Cowan, and J. Saunders, Phys. Rev. Lett. **81**,115301 (2003).
[2] G. Misguich, B. Bernu, C. Lhuillier, and C. Waldtmann, Phys. Rev. Lett. **81**,1098 (1998).
[3] K. Ishida, M. Morishita, K. Yawata, and H. Fukuyama, Phys. Rev. Lett. **79**, 3451 (1997).
[4] R. Masutomi, Y. Karaki, and H. Ishimoto, Phys. Rev. Lett. **92**, 025301 (2004).

Authors
A. Yamaguchi, H. Nema, Y. Tanaka, and H. Ishimoto

Development of Implosive Magnet Coils for Mega-gauss Magnetic Field Generation

Takeyama Group

The magnetic field over 100 Tesla can be attained only by a destructive pulsed magnet. There are three kinds of destructive pulsed magnets for the generation of such an ultrahigh magnetic field (the single turn coil [1], the explosive-driven flux compression [2], the electro-magnetic flux compression (EMFC) [3-5]). Although one can generate ultrahigh magnetic field with the inner sample space intact by the single turn coil method, the maximum field is limited to about 300T for a reasonable bore radius. The explosive-driven flux compression or the electro-magnetic flux compression can generate much higher field than the single turn coil in spite of complete destruction of the substances in the sample space after the field generation. Explosive-driven flux compression can generate the highest magnetic field. However, there are limitations in the application to measurements for solid-state physics because the necessary use of up to 200 kilograms of explosives results in total destruction of all equipment placed within a few meters from the magnet. Electro-magnetic flux compression is more suitable for measurements of solid-state physics than explosive-driven flux compression because the destruction is limited to a relatively small space, and can be placed in a indoor space.

The EMFC was originally developed by E. Cnare [3]. The EMFC system at ISSP has been developed since the early 1970s. This system is now acknowledged as generating the world-highest field (622 T) as an indoor system [5]. It has been served to various measurements of solid state physics in ultrahigh magnetic fields. Recently, a group at Loughborough University developed the EMFC system by using a fast condenser bank system which was normally used for the single turn coil method. They reported the success of generating over 300T [6].

The EMFC system consists of a primary coil and a liner ring (a liner). We have recently conducted successful improvement for the primary coil system to generate higher field with less energy injection and with more simplified coil preparation processes. Steel has been adopted as a material for the primary coils for a long time at ISSP. Two technical problems are inherent in the old type primary coil. One is a structural problem. The old coil consists of three separated parts (one of a coil part and two of upper and lower electrodes). A small gap near the junction is unavoidable because of the inadequate geometrical contact due to the coil structure (see the top picture at the left side of Fig.1). This gap can bring an undesirable electric discharging during the primary current injection. We have found that such a spark discharging is an important factor for the reduction of the energy transfer efficiency and for emission of electro-magnetic noise. Another is the problem on the material itself. The old coil is made of steel which has a high electrical resistance and accordingly renders a deep high-frequency current skin depth. A high electrical resistance reduces efficiency of the electro-magnetic energy transfer. The deep skin depth serves as increase of the effective feed-gap, which is unfavorable for the liner symmetrical implosion.

To solve these problems, we changed the structure and the material of the primary coil. A new coil system has a bended cupper sheet inside a steel coil (see the top picture at the right side of Fig.1). In the new coil system, the cupper

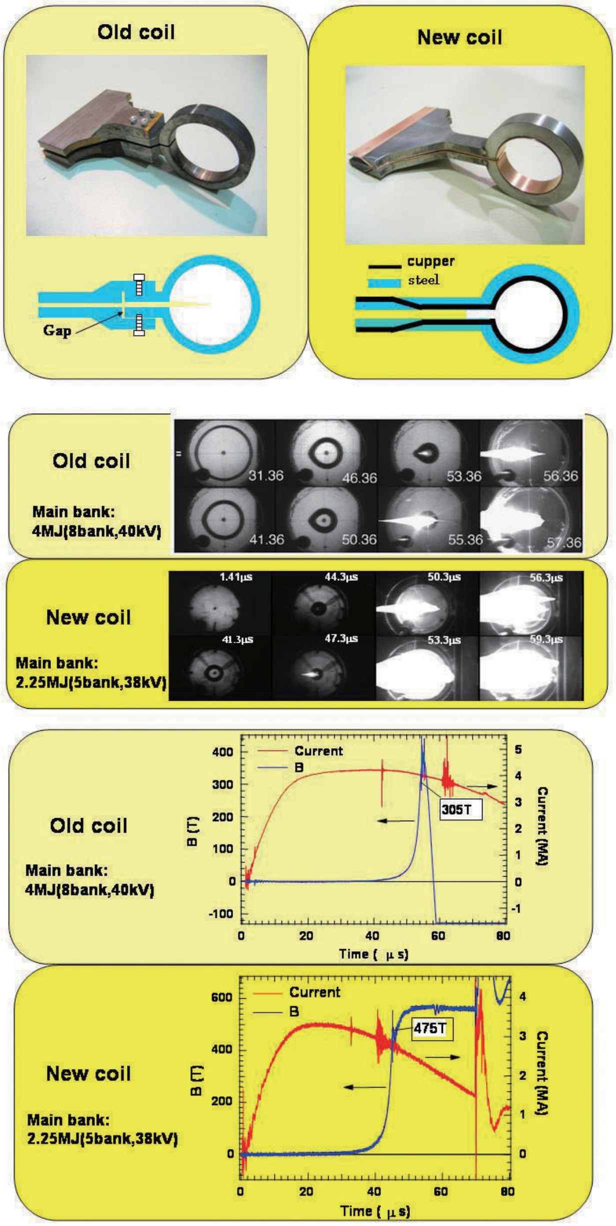

Fig. 1. A comparison of the new and old coil used for the EMFC at ISSP. From top to the bottom; the primary coil structure, the high speed photograph of the liner implosion, the primary current and the magnetic field.

sheet beers the main primary current flow. The shape of cupper sheet is specially designed to improve the electric contact with an electrode of the current collector plate from the condenser bank. Cupper has 1/9 times smaller resistance and 1/3 times shallower skin depth than steel. The role of the steel coil in the present coil system is different from that in the conventional old type coils. The steel coil in the new coil is designed for a provision of mass to avoid a deformation of cupper sheet during an acceleration of the liner.

We performed the EMFC experiments by using the new coil system. The bottom of Fig.1 shows a comparison of the magnetic field and the primary current between a new coil and an old coil. The new coil system could generate up to 475 T by a 2.3 MJ energy injection (the maximum primary current 3.2MA). This is a remarkable progress from the old system, in which 350 T was obtained with 4 MJ (the maximum primary current 4.2 MA). It is evident that the electro-magnetic energy transfer efficiency has been improved a great deal by employing a new coil system.

The effect of feed-gap in a new coil system was reduced as we expected. The middle of Fig. 1 shows the high speed photograph of the liner implosion, where the effect of a feed-gap was pronounced in an old coil, whereas the effect was much reduced in a new coil. The cylindrical symmetry of the liner implosion was comparable even with that by adopting “the feed-gap compensator”, which has recently attained a great success to record the highest magnetic field up to 622 T [6].

In the high field generation by the flux compression, the most important factor is a velocity of the liner implosion. There is a definite correlation between the velocity of the liner implosion and the maximum field [6]. The velocity of inner radius of the liner was estimated from the high speed photograph of Fig.1. In the new coil, the estimated velocity was 2.4 km/s which was the fastest record ever obtained at ISSP. The rising time of the field was also the shortest, which supports the fastest implosion of a liner.

In our recent experiments by using a newly designed coil, a pick up coil for the field detection was unfortunately destroyed by a luminous jet before the field reached the maximum. We are convinced, however, that the new system is promising for generation of higher fields than those recorded ever before by the EMFC techniques.

References

[1] N. Miura *et al*., Physica B **294-295**, 562 (2001)
[2] C. M. Fowler, W.B. Garn, and R. S. Caird, J. Appl. Phys. **31**, 588 (1960)
[3] E.C. Cnare, J. Appl. Phys. **37**, 3812 (1966)
[4] F. Herlach *et al*., IEEE Trans. Nucl. Sci. NS-**18**, 809 (1971)
[5] M. H. Matsuda *et al*., Rev. Sci. Inst. **73**, 4288 (2002)
[6] B. M. Novac, I. R. Smith, D.F. Rankin, and M. Hubbard, J. Phys. D: Appl. Phys. **37**, 3041(2004)

Authors
E. Kojima and S. Takeyama

Interlayer Coupling and Magnetotransport in Layered Conductors

Osada Group

Low-dimensional layered conductors, which include organic conductors, layered oxides, intercalation compounds, artificial superlattices, *etc*., show rich magnetotransport features as a function of magnetic field orientations. The most remarkable examples are angle-dependent oscillations or resonances, such as AMRO (Yamaji oscillations) in quasi-2D conductors or Lebed resonances in quasi-1D conductors. Usually, the background of interlayer resistance, on which angle-dependent oscillations or resonances superpose, takes a local maximum when the field is parallel to layers, since the Lorentz force works most effectively. Sometimes, a sharp peak structure superposes at the parallel field orientation (peak effect). These phenomena have been believed to be bulk effects originating from electron orbital motion on the Fermi surfaces. On the other hand, some layered conductors show anomalous background taking a local minimum at the parallel orientation. The origin of this "background inversion" has been an open question.

Does the angle-dependent interlayer magnetotransport in layered conductors truly originate from bulk effects? What causes the background inversion? To answer these questions, we have performed experimental tests using GaAs/Al$_x$Ga$_{1-x}$As artificial multilayer systems with

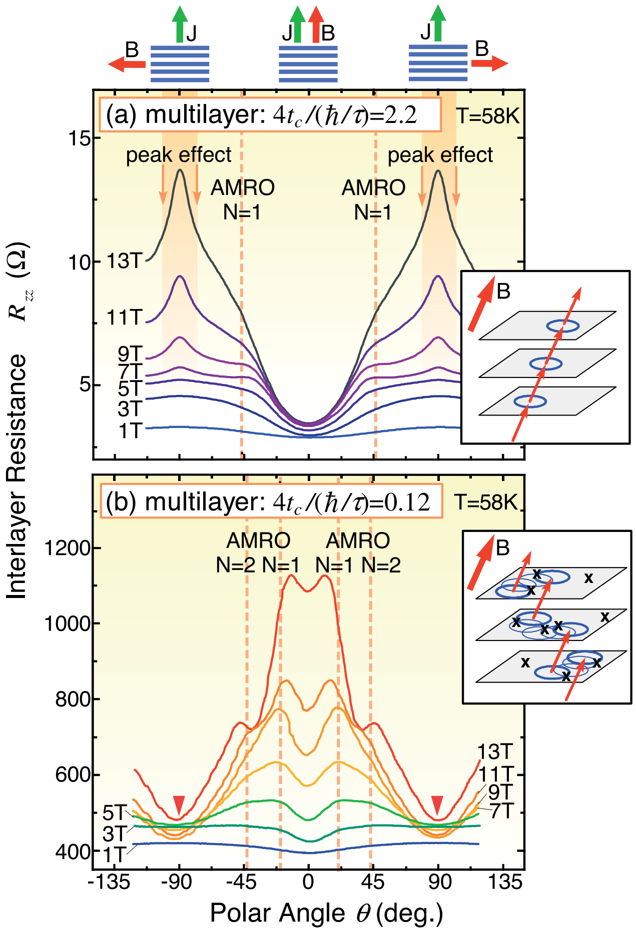

Fig. 1. Interlayer resistance of GaAs/Al$_x$Ga$_{1-x}$As multilayers for different field orientations. The angle-dependent features dramatically change depending on the ratio of interlayer tunneling rate and in-plane scattering rate.

controlled structures and parameters.

In the first test, we have changed the strength of interlayer coupling in GaAs/Al$_x$Ga$_{1-x}$As superlattices to simulate "clean" and "dirty" layered conductors. In the "dirty" samples, in-plane scattering occurs more often than interlayer tunneling due to small interlayer coupling, and the interlayer mean free path is much shorter than the interlayer spacing. As shown in Fig. 1, we have found that the background inversion occurs only in the "dirty" samples. This is the first experiment which has related the background inversion to interlayer coupling. We have also found that AMRO survives even in the "dirty" samples, while the peak effect vanishes.

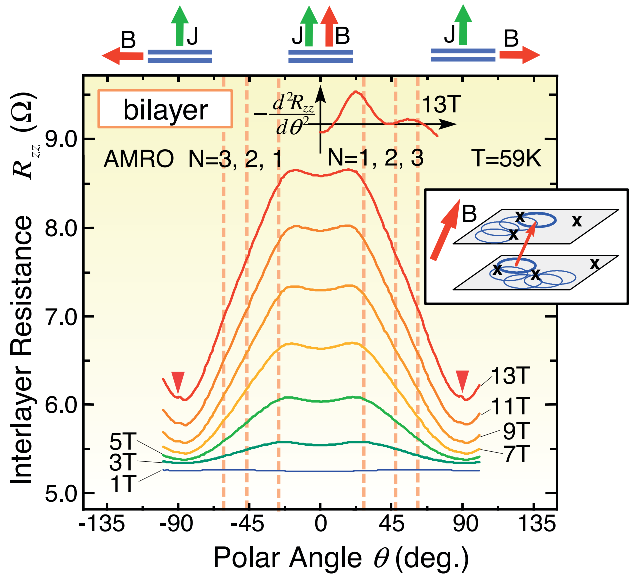

Fig. 2. Interlayer resistance of a GaAs/Al$_x$Ga$_{1-x}$As bilayer system for different field orientations. We can conclude that the features observed also in a bilayer originate from local mechanism.

In the next test, we have reduced the number of layer to distinguish local effects from bulk effects. The bulk effects originating from electron orbital motion should be strongly suppressed in a few layer samples. As shown in Fig. 2, we have found that the background inversion occurs even in the "dirty" systems with a few layers, and that AMRO still survives even in a few layers ("clean" and "dirty"), but that the peak effect vanishes in a few layers.

From these results, we can conclude that AMRO originates not from the electron orbital motion on the Fermi surfaces but from the local interlayer tunneling between two neighboring layers. On the other hands, the peak effect is a bulk effect due to electron orbital motion. We can also conclude that the background inversion is a local phenomenon in the "dirty system", which might originate from in-plane diffusion.

Authors
T. Osada, M. Kobayakawa, K. Kuraguchi, and E. Ohmichi

Charge-Transfer Phase Transition of Iron Mixed-Valence Complex $(n\text{-}C_3H_7)_4N[Fe^{II}Fe^{III}(dto)_3]$

Uwatoko Group

The iron mixed-valence complex, $(n\text{-}C_3H_7)_4N[Fe^{II}Fe^{III}(dto)_3]$ (dto = dithiooxalato $C_2O_2S_2$) shows a charge-transfer (CT) phase transition at T_{CT} = 122.4 K. In the vicinity of T_{CT}, the spin state changes from Fe^{II} (S = 2) – Fe^{III} (S = 1/2) (high-temperature phase: HTP) to Fe^{II} (S = 0) – Fe^{III} (S = 5/2) (low-temperature phase: LTP) accompanied by a charge-transfer between Fe^{II} and Fe^{III}. This complex also undergoes a ferromagnetic transition at 7 K in the LTP. The ferromagnetic interaction takes place over a long distance involving Fe^{III} (S = 5/2) - $S_2C_2O_2$ - Fe^{II} (S = 0) - $O_2C_2S_2$ - Fe^{III} (S = 5/2). The ferromagnetic ordering is presumably induced by the charge-transfer interaction between Fe^{II} and Fe^{III} [1].

The most remarkable point of CT transition in $(n\text{-}C_3H_7)_4N[Fe^{II}Fe^{III}(dto)_3]$ is, that the result of heat capacity measurements enable us to speculate that the spin-entropy drives the CT phase transition [2]. Therefore, the cooperative effect between a metal ion and lattice strain is extremely small, compared to typical spin crossover complex [3].

We chased the structural changing around CT phase transition by high-resolution powder x-ray diffraction (PXD) at Spring-8 BL02B2. At CT phase transition, abrupt constriction was observed in 2-D honeycomb network layer $[Fe^{II}Fe^{III}(dto)_3]$- (*ab* plane). For *c* axis, monotonous constriction was observed between 20 K and 300 K. As a result, small volume change was observed at CT transition. Fundamentally it is considered that abrupt constriction of *ab* plane induces the electron-transfer between iron atoms. From the result of Rietveld analysis, a volume constriction of $[FeS_6]$ octahedron and a volume expansion of $[FeO_6]$ in $[Fe^{II}Fe^{III}(dto)_3]$ were observed at 120 K, it is revealed that these two conflicting vibration entropy cancel out each other, as a result, the cancellation appears as origin of the small excess entropy beyond the contribution from change in the

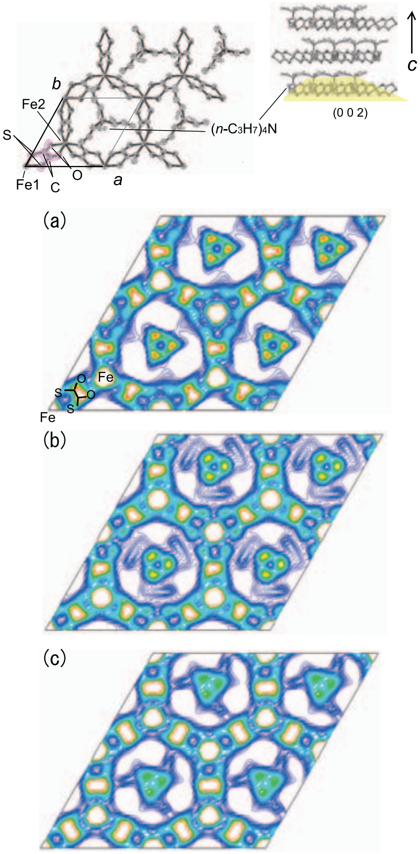

Fig. 1. Crystal structure of $(n\text{-}C_3H_7)_4N[Fe^{II}Fe^{III}(dto)_3]$ with [002] section (left) and projection of [110] (right).(a) MEM charge density of [0 0 2] section at 180 K, (b) 120 K, (c) 90 K. Counter lines are drawn between 0.0 and 1.0 e/Å^3 with 0.001 e/Å^3 intervals. The total charges of Fe1 and Fe2 are estimated as 24.51 *e* and 25.23 *e* (at 180 K), 24.70 *e* and 24.69 *e* (120K) and 24.38 *e* and 23.26 *e* (at 90 K), respectively.

spin multiplicity.

The electron density distributions around CT transition have been succeeded in carrying out by the maximum entropy method (MEM) combined with Rietveld method. Figure 1 shows the MEM charge density of [0 0 2] section at (a) 180 K, (b) 120 K, (c) 90 K. Counter lines are drawn between 0.0 and 1.0 e/Å^3 with 0.001 e/Å^3 intervals. The strong covalent bonding of sulfur atoms clearly appears with widely distributed electrons, compared to the density around oxygen bonding. The total charges of Fe1 and Fe2 are estimated as 24.51 *e* and 25.23 *e* (at 180 K), respectively. At 120 K, the charge distribution on dto molecules expands in whole honeycomb ring, at this point, the charge of Fe1 and Fe2 take almost same values of 24.70 *e* and 24.69 *e*. At 90 K, the honeycomb ring shrank, the charge on two Fe1 and Fe2 became 24.38 *e* and 23.26 *e* (at 90 K). We can clearly describe the electron transfer between Fe^{II} and Fe^{III} at CT phase transition by x-ray structure analysis.

$(n\text{-}C_3H_7)_4N[Fe^{II}Fe^{III}(dto)_3]$ is very sensitive for external pressure. The T_{CT} increases linearly with applied pressure, the T_{CT} close to room temperature under 1 GPa [4]. We also investigated the structural change of $(n\text{-}C_3H_7)_4N[Fe^{II}Fe^{III}(dto)_3]$ under high pressure using diamond anvil cell (DAC) at Spring-8 BL10XU. The tendency of structural change is deferent from that of ambient pressure. Under high pressure, on cooling an abrupt constriction of *ab* plane was observed at CT transition. However, on heating, we observed abrupt expansion of c axis. No abrupt expansion of *ab* plane was observed on heating. As a result, small cell volume change was observed at the CT transition under pressure.

In summary, by high-resolution PXD and PXD under pressure, we revealed that the organ of CT phase transition is a small volume change and spin-entropy difference between HTP and LTP. We have also succeeded in direct observation of electron-transfer between iron atoms at CT transition.

References

[1] N. Kojima, W. Aoki, M. Itoi, Y. Ono, M. Seto, Y. Kobayashi, and Y. Maeda, Solid State Commun. **120**, 165 (2001)
[2] T.Nakamoto, Y. Miyazaki, M. Itoi, Y. Ono, N. Kojima, M. Sorai, Angew. Chem. Int. Ed. **40**, 4716 (2001)
[3] M. Sorai and S. Seki, J. Phys. Chem. Solids. **35**, 555 (1974) .
[4] Y. Kobayashi, M. Itoi, N. Kojima, and K. Asai, J. Phys. Soc. Jpn. **71**, 3016 (2002)

Authors

M. Itoi, C. Lin, M. Koeda, M. Hedo, Y. Uwatoko, N. Kida[a], N. Kojima[a], Y. Kobayashi[b], K. Asai[b], K. Kato[c], K. Osaka[c], Y. Ohishi[c], M. Takata[c]
[a]Graduate School of Arts and Sciences, The University of Tokyo
[b]Department of Applied Physics and Chemistry, University of Electro-Communications
[c]Spring-8/JASRI

Investigation of $YbInCu_4$ at Pressures to 7 GPa

Uwatoko Group

It is well-known that $YbInCu_4$ shows a first order isostructural valence transition at $T_V \sim 40$ K [1], above which Yb is in a magnetic state of Yb^{3+}, while below which it is non-magnetic Yb^{2+}. In addition, it is found that the valence transition is suppressed with applying pressure and disappears with further pressurization. In previous work, we found an anomalous decrease of the resistivity at $T \sim 1.4$ K under several pressures, which led us to speculate the occurrence of a superconducting state under pressure [2]. On the other hand, Mito *et al.* [3] recently found that a ferromagnetic state is induced together with the disappearance of the valence transition upon pressurization. Therefore, much attention has been paid to how the electrical system behaves under pressures after the valence transition disappears. To elucidate a pressure-induced phase at the lowest temperatures, electrical resistivity measurements have been performed under higher pressures.

We have newly developed a novel diamond anvil cell

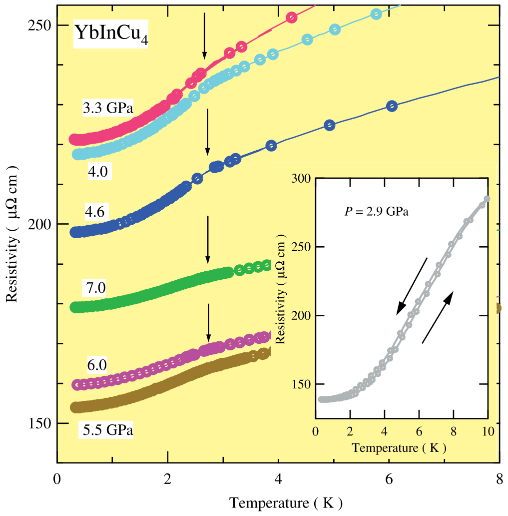

Fig. 1. Temperature dependence of the electrical resistivities of $YbInCu_4$ at low temperatures and at representative pressures. Arrows indicate the temperature where there is a ‘knee’ in ρ(T). The inset shows the resistivity under 2.9 GPa.

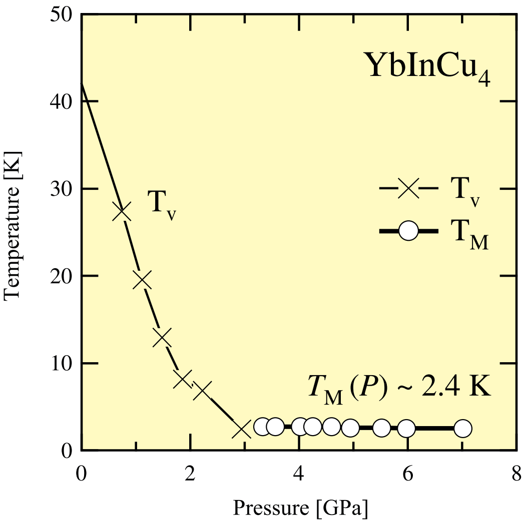

Fig.2. The temperature-pressure phase diagram for YbInCu$_4$. Cross marks and open circles indicate the valence transition temperature T_v and some transition temperature T_M, respectively. T_M is almost constant at 2.4 K for high pressures.

designed to perform high pressure electrical transport measurements based on the concept of a turnbuckle. This pressure apparatus, with a 1:1 mixture of Fluorinert FC70 and FC77 as the pressure-transmitting medium, was used in this work.

Electrical resistivity measurements were performed under $2.9 < P < 7.0$ GPa and for $300 < T < 0.3$ K. Figure 1 shows the temperature dependence of the electrical resistivity of YbInCu$_4$ at low temperature for P = 3.3, 4.0, 4.6, 5.5 6.0, 7.0 GPa. As shown in the inset in Fig. 1, the resistivity at P = 2.9 GPa exhibits a hysteresis near the valence transition temperature T_v ~ 6.2 K. For $P \geq 3.3$ GPa, the valence transition disappears, with no detectable hysteresis at low temperatures. As is recognizable from Fig. 1, the resistivity at low temperature is suppressed by increasing pressure from 3.3 GPa to 5.5 GPa and enhanced with applying higher pressure. We tentatively fit the data obtained in the previous and this work at low temperature to $\rho = \rho_0 + AT^2$. Both the residual resistivity ρ_0 and the resistivity coefficient A as a function of pressure show broad peaks around 4 GPa as expected in ref. [2]. This suggests that YbInCu$_4$ around 4 GPa may be in the vicinity of a quantum critical point, given the report of similar variations of A and ρ_0 in the pressure-induced superconductor CeCu$_2$Ge$_2$ [4]; although, P-induced changes in carrier density and ground-state degeneracy could provide an alternative interpretation [5].

In this work, slight decreases of the resistivities, indicated by arrows in Fig. 1, are observed at T_M ~ 2.4 K that is independent of pressures from 3.3 GPa up to 7.0 GPa. These decreases were also found by T. Mito et al who concluded that T_M signaled a paramagnetic to pressure-induced ferromagnetic state [3]. A temperature-pressure phase diagram up to 7.0 GPa is shown in Fig. 2. The diagram is different from that of Mito *et al.* in terms of the pressure dependence of T_V and T_M. Moreover there is no explanation for why T_M hardly changes with applying pressure.

In conclusion, electrical resistivity measurements of YbInCu$_4$ by a four-wire method was performed under $2.9 < P < 7.0$ GPa down to 0.3 K. We have clarified that YbInCu$_4$ around 4 GPa may be near a quantum critical point and that an anomalous transition appears at T_M ~ 2.4 K above 3.3 GPa where the valence transition has vanished. Various kinds of measurements, including resistivity in more detail around 4 GPa, may enable us to better understand the essential physical properties of YbInCu$_4$.

References

[1] I. Felner *et al*., Phys. Rev. B **33**, 617 (1986).
[2] M. Hedo et al., Acta Phys. Pol. B **34**, 1193 (2003).
[3] T. Mito *et al*., Phys. Rev. B **67**, 224409 (2003).
[4] D. Jaccard *et al*., Physica B **259-262**, 1 (1999).
[5] T. Park *et al*., Phys. Rev. Lett. **96**, 046405 (2006).

Authors

N. Kurita, M. Kano, M. Hedo, Y. Uwatoko, J. L. Sarrao[a], J. D. Thompson[a], and S. W. Tozer[b]
[a]Los Alamos National Laboratory
[b]National High Magnetic Field Laboratory

Selective Observation of the Nuclear Wave-packet Dynamics in the Excited State

Suemoto Group

The dynamics of atoms or molecules in condensed matters is an important issue for understanding the chemical processes, defect formation and phase transitions, and also for controlling the photo-induced phase transitions [1]. The local motions of atoms are suitably described in terms of a nuclear wave-packet (WP) propagating on the adiabatic potential-energy surfaces (APEs).

Up to now, the WP dynamics has been studied most widely by means of transient absorption or reflection spectroscopy using femtosecond laser pulses. However, it has been difficult to separate the effects of absorption to higher electronic states and induced emission to the ground state. In addition, the discrimination between the dynamics in the ground state and the excited state has also been difficult. In contrast, the femtosecond luminescence spectroscopy allows us to solve these problems.

Here, we demonstrate a definitive difference between the ground- and excited-state dynamics by comparing our luminescence experiment [2] with the pump-probe ones by Nisoli *et al.* [3] at the F center in KBr, which is a prototype of an optical center with strong electron-lattice interactions. Figure 1 shows the time evolution of the luminescence

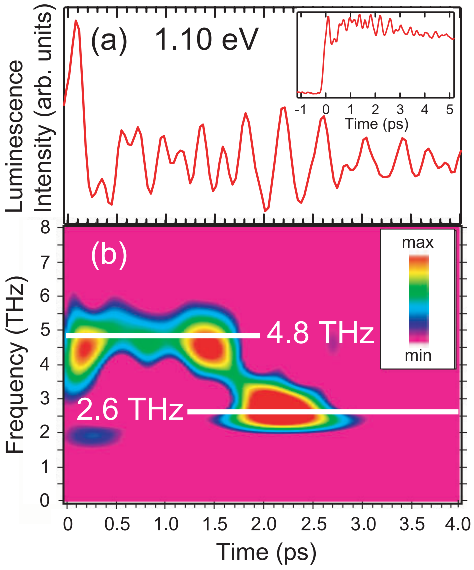

Fig. 1. Time evolution of the luminescence intensity at 1.10 eV and its continuous wavelet transform. (a) The oscillating component in the 0-4 ps delay range. The inset shows the original wave form. (b) Continuous wavelet transform of (a). The color scale indicates the signal amplitude, red being the maximum.

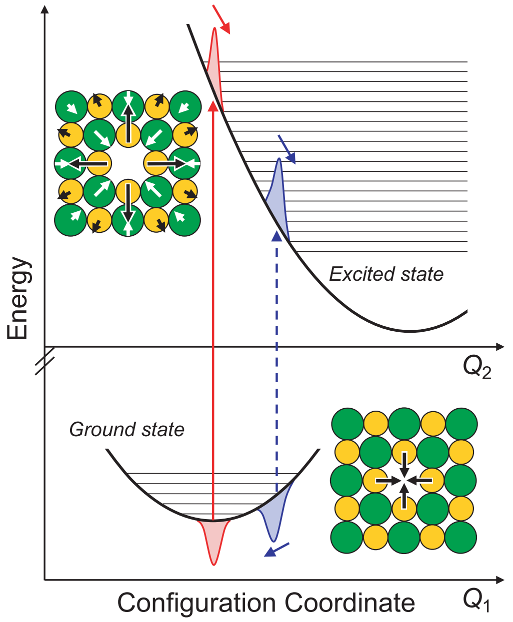

Fig. 2 The red and blue upward arrows connecting two APESs show the Franck-Condon transitions in our luminescence measurement and the pump-probe ones by Nisoli *et al*., respectively. In the cross-section drawings of the lattice around the *F* center, the green and yellow circles represent halogen and alkali ions, respectively. The solid arrows represent the direction of the coherent movements of neighboring ions just after photoexcitation.

intensity observed at 1.10 eV (a) and its wavelet analysis showing the time-dependent Fourier power spectrum (b). The oscillation reflects the WP motion on the APES. In contrast to the transient absorption measurements, in which they observed a pronounced peak at 3.3 THz [3], we observed two peaks at 2.6 and 4.8 THz as seen in Fig. 1(b).

The situation is explained in Fig. 2. An optical pulse excitation creates the WP as a coherent superposition of the vibrational wave-functions on the APESs. As the pump-probe measurements described in [3] were performed under off-resonant excitation (blue case in Fig. 2), the optical excitation initiated the swinging of the negative WP along the ground-state APES. Since the probe pulse energy is close to the pump pulse one, the probe signal reflects mainly this phenomenon (lower illustration in Fig. 2). The wave-function of the ground state is compact and interacts strongly with a local breathing mode, *i.e.*, A_{1g} mode at 3.3 THz. On the other hand, the luminescence measurement was performed under resonant excitation from the bottom of the APES (red case in Fig. 2), and the detected photon energy of 1.10 eV is far from the absorption band. Thus, the result reflects solely the WP dynamics in the excited state (upper illustration in Fig. 2). In the excited state, the electronic wave-function spreads out, so that the electron preferably couples to the bulk phonon modes LA and LO, which peak at 2.6 and 4.8 THz, respectively. Our result clearly shows that the WP in the ground state and that in the excited state have significantly different character and that the luminescence method has an advantage in studying the *WP dynamics in the excited state*.

References

[1] K. Nasu *et al*., in *Photoinduced Phase Transitions*, edited by K. Nasu (World Scientific Publishing, Singapore, 2004).
[2] T. Koyama, Y. Takahashi, M. Nakajima, and T. Suemoto, Phys. Rev. B **73**, 161102(R) (2006).
[3] M. Nisoli *et al*., Phys. Rev. Lett. **77**, 3463 (1996).

Authors

T. Koyama, Y. Takahashi, M. Nakajima, and T. Suemoto

Development of Highly Advanced Soft X-Ray Lasers and its Applications

Kuroda Group

Since the time when first ruby laser was demonstrated, future development of x-ray laser remains as one of a dream of laser physicists and almost all researchers engaged in laser applications involving biomedical applications and basic medicine. We have developed the new 18.9 nm Ni-Mo x-ray laser based on the transient-collisional-excitation (TCE) scheme extended to the Ni-like ion, which has extraordinary small divergence and also operates with only 150 mJ pump laser energy [1,2]. These are over ten times good divergence and 100 times smaller energy compared to other results. This method uses a sub-picosecond or femtosecond, high-intensity laser pulse to generate a short-lived, high gain laser medium of only 2 mm length within preformed plasma. The experimental results reveal an additional favorable characteristic of longitudinal-pumped TCE x-ray laser, *i.e*., ultra-small divergence of less than one milliradian (0.3 mrad). These unique features will have a large impact on x-ray laser application. An example is the precise measurement of time-resolved emission spectroscopy in live tissue, which is tremendously difficult even with advanced synchrotron radiation sources, and we hope to renew our understandings of new fields such as nanotechnology, nanobiology, and laser medicine. Efforts to develop shorter wavelength around "water window" region (2.2 nm-4.4 nm) based on Ni-W 4.3 nm laser will be continued.

We show the intensity trace of a typical on-axis soft-x-ray spectrum between 15 and 25 nm observed using TCE experimental setup in Fig.1. The background originating from the noise of the detector was subtracted to obtain the actual spectral intensity trace. The pump laser energy in the long and short pulse is only 30 mJ and 120 mJ. The localization of the Ni-like ion abundant occurred at the region of the longitudinal beam. Simulations show that the 1.5×10^{11} W cm^{-2} intensity pre-pulse is only capable of

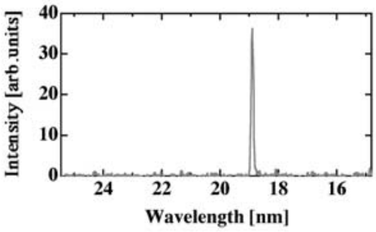

Fig. 1. Intensity trace of the on-axis soft-X-ray spectrum between 15 and 25 nm. The background was subtracted from the trace to obtain the actual intensity profile.

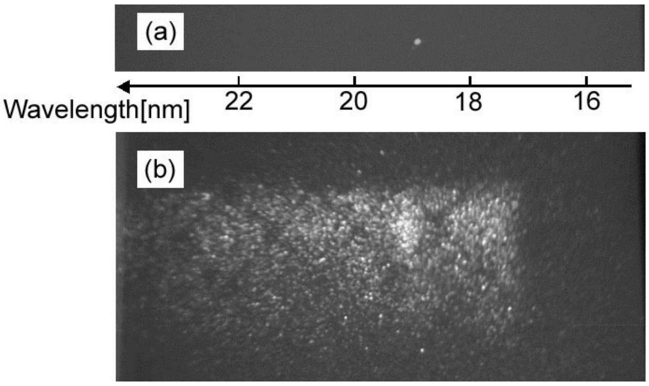

Fig. 2. Spectrum image of the on-axis emission for plasma length of (a) 2.0 mm and (b) 0.5 mm. The sensitivity of the photocathode camera was increased by about eight times for (b).

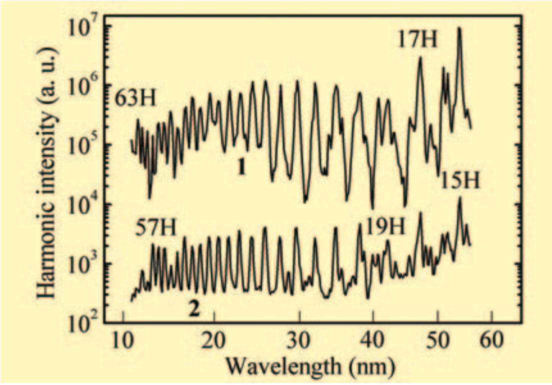

Fig. 3. Harmonic output from B plasma as a function of the wavelength of generated XUV radiation in the cases of (1) orthogonal and (2) longitudinal pump schemes.

producing pre-plasma with an average ionization of 8, much less than 14 required for Ni-like molybdenum ions. However, by introducing a 300 ps duration, 1×10^{-5} contrast ratio pedestal to the main pulse, the temperature and density is increased to 90 eV and 1×10^{20} cm^{-3}. As a result, narrow Ni-like molybdenum abundant region is produced in the pre-plasma, which can generate high gain with the irradiation of the high intensity main pump.

We are also devoting extensive studies on higher harmonic generation from solid surface plasma, which is also recognized as an alternative way to pursue coherent light source in soft X-ray regions. The availability of compact, high-intensity sub-picosecond lasers with chirped pulse amplification (CPA) has opened the new field of study for laser-matter interactions with solid targets. At the high laser intensities above 10^{16} Wcm^{-2}, the electron temperature is more than one keV and the main laser absorption is related to collisionless absorption. Collisionless absorption mechanisms include vacuum heating, $J \times B$ heating, sheath inverse Bremstrahlung, and the anomalous skin effect. These results are important demonstrations of the large harmonic blue shift that can provide a tool to realize a tunable coherent subpicosecond light source. We observed an interesting blue shift of generated higher harmonics without broadening due to self phase modulation. These shifts are brought about by collisionless absorption process, which shows an onset of new interaction process predicted for a mechanism responsible for ultra short and intense, laser-matter interaction [3].

The high-order harmonic generation (HHG) from the interaction of ultrashort laser pulses with gas jets and solid targets has proven to be an effective source of coherent short-wavelength radiation. The HHG in visible and extreme ultraviolet (XUV) ranges has been investigated using the laser plasma formed by an optical breakdown in gases and at the surface of solid targets. The method for generating harmonics from solid target atoms apart from solid surface is based on the preparation of a gas-like ablation plume via laser-surface interaction with further propagation of short laser pulse through this medium. The application of various ions provided important information on their role for the HHG. However, the maximum observed order of harmonics reported in those studies was limited to the 27th one due to some concurred effects in high-excited plasma. The peculiarity of the harmonic generation from the surface plasma with comparing to the conventional gas-jet technique includes its capability of generating the plasma with high density, long length, and variable conditions of plasma excitation. This technique also gives new degrees of freedom that can be used to optimize the HHG. The use of any elements in the periodic table that can be formed as solid targets may disclose many interesting peculiarities for the generation of coherent XUV radiation. The optimization of plasma conditions can lead to further growth of HHG efficiency. In particular, the low-excited plasma could possess some attractive properties in comparison with high-excited ones (*i.e.*, less reabsorption of generated harmonics, less influence of free electrons on phase-matching and self-defocusing, etc.) that can increase both the conversion efficiency and cutoff energy of harmonics. We demonstrated the efficient generation of coherent XUV radiation after the propagation of femtosecond pulse through the low-excited plasma produced on the surface of different solid targets. We showed the high harmonics up to the 65th order (λ=12.6 nm) using B target in Fig.3 and the conversion efficiencies at the plateau region up to 8×10^{-6} were achieved [4].

References

[1] T. Ozaki, H. Kuroda *et al.*, Phys.Rev.Lett. **89**, 252902 (2002).
[2] H. Kuroda, M. Suzuki, R. A. Ganeev, M. Baba *et al.*, Proc. of 9th International Conference on X-ray lasers, I2802 (2004).
[3] A. Ishizawa, T. Ozaki, R. A. Ganeev, and H. Kuroda, Phys. Rev. E. **66**, 026414 (2002).
[4] R. Ganeev, M. Suzuki, M. Baba, H. Kuroda, T. Ozaki, Opt. Lett. **30**, 768 (2005).

Authors

H. Kuroda, M. Baba, M. Suzuki, R. A. Ganeev, and T. Ozaki[a]
[a]Institut National de la Recherche Scientifique, Canada

Low-Threshold Single-Mode Current-Injection Lasing in T-shaped GaAs Quantum Wire Lasers

Akiyama Group

Quantum-wire lasers are expected to exhibit superior performance to conventional semiconductor lasers due to their one-dimensional electronic states. However, such performances have not yet been realized most likely because of difficulty in preparation of homogenous quantum-wire structures. Recently we fabricated GaAs T-shaped quantum wires (T-wires) with high interface homogeneity by cleaved-edge overgrowth with molecular beam epitaxy, and reported lasing by optical excitation and basic one-dimensional optical properties [1-3]. The first current-injection T-wire laser was reported in 1994 [4], where multimode lasing occurred with 0.4 mA-0.8 mA thresholds at 4 K, but there has been no report since then. In this year, we demonstrated low-threshold current-injection single-mode lasing at 30-70 K based on a new simple current-injection scheme. At 30 K, threshold current was 0.27 mA and differential quantum efficiency was 17%.

In our laser sample, 20-period GaAs quantum wires (T-wires) are formed at T-shaped intersections of 20-layers of 14-nm-thick stem wells and a 6-nm-thick arm well. The T-wires are embedded in the core of the T-shaped optical waveguide surrounded by the cladding layers. Since Si-doped (C-doped) multiple quantum wells (MQWs) are formed as an n-type (p-type) injection layer on the bottom (top) of the stem slab waveguide, both electrons and holes are injected into the arm well and then flow into the T-wires. We call this new injection scheme as arm-arm injection. A laser bar with 500 μm cavity length was cut from the wafer

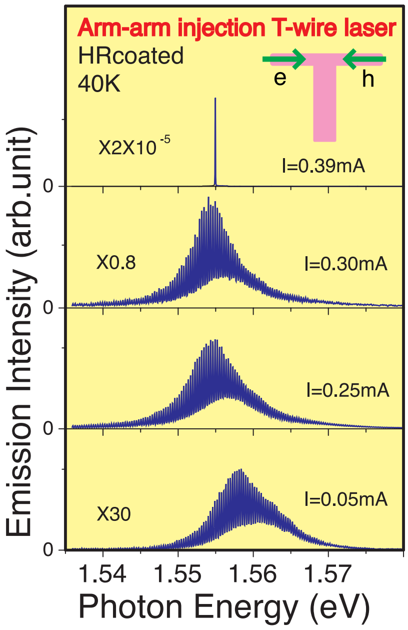

Fig. 1. High-resolution emission spectra of the 500 μm-long quantum-wire laser at four input currents.

by cleavage, and the cavity facets were coated with 50-nm-thick (front facet) and 200-nm-thick gold films.

Emission spectra of the laser at 40 K for four injected currents are shown in Fig.1. As the current injection increases, the emission band narrows showing red-shifts, and finally reaches stable single-mode lasing. Single-mode lasing is similarly observed at all cryostat temperatures between 30 K and 70 K. Figure 2 (a) shows the corresponding output power vs. input current. The threshold current and differential quantum efficiency vs. temperature are depicted in Fig.2 (b). At 30 K, we observe the lowest threshold current of 0.27 mA and the highest differential quantum efficiency of 17%. As the temperature is increased, we observe higher threshold current and lower differential quantum efficiency. At lower temperatures than 30 K, we do not observe single mode lasing. The current vs. voltage (IV) characteristic at temperatures below 30 K shows rather high series resistance, probably due to carrier freezing in C-doped and/or Si-doped GaAs MQW layers.

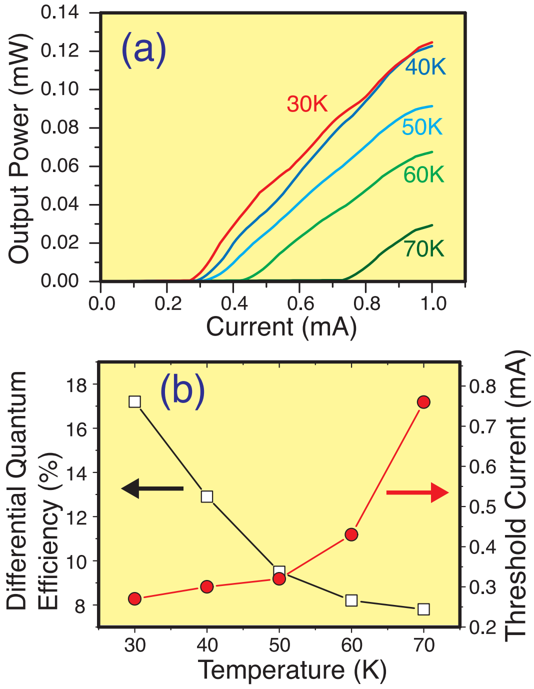

Fig. 2. (a) Light output vs. input current for a quantum wire laser. (b) Threshold current and differential quantum efficiency vs. temperature.

Micro-photoluminescence study on the same sample has demonstrated very high uniformity of quantum wires, to which the low lasing threshold is firstly ascribed. We studied carrier-injection behavior in this structure by luminescence imaging, and found that significant portion of carriers overpass the wire region without recombination. This suggests that improvement in the doping design should further improve threshold current and quantum efficiency of the present laser.

References
[1] Y. Hayamizu, *et al*., Appl. Phys. Lett. **81**, 4937 (2002).
[2] H. Akiyama, *et al*., J. Phys. Condensed Matter **16**, S3549 (2004).
[3] Y. Takahashi, *et al*., Appl. Phys. Lett. **86**, 243101 (2005).
[4] W. Wegscheider, *et al*., Appl. Phys. Lett. **65**, 2510 (1994).

Authors
Shu-man Liu, M. Yoshita, M. Okano, T. Ihara, H. Itoh, H. Akiyama, L. Pfeiffer[a], K. West[a], and K. Baldwin[a]
[a]Bell Laboratories, Lucent Technologies, USA

Developments of FZP Beam Profile Monitor

Nakamura Group

The FZP (Fresnel zone plate) beam profile monitor constructed at the KEK-ATF damping ring is a real-time and high-resolution monitor using an X-ray imaging optics based on two FZPs. In the monitor beamline, the synchrotron radiation from the electron beam is monochromatized by a crystal monochromator and the transverse beam image is twenty-times magnified by the two zone plates (CZP and MZP) and detected on the X-ray CCD camera. This monitor can take real-time images of the electron beam and measure the beam profiles and sizes with a high spatial resolution of less than 1 μm. Clear electron-beam images with the vertical beam sizes less than 10 μm were successfully observed with this monitor [1].

Recently the FZP beam profile monitor was greatly improved [2]. The new monochromator was made in order to suppress the angle drift of the crystal. In the new monochromator, the stepping motor was thermally isolated from the main part of the monochromator by ceramic insulators and thermally stabilized by copper lines cooled by the water. The FZP holders were newly designed and fabricated so that the FZPs could be inserted in and removed from the optical path in the vacuum when necessary. A precise beam-based

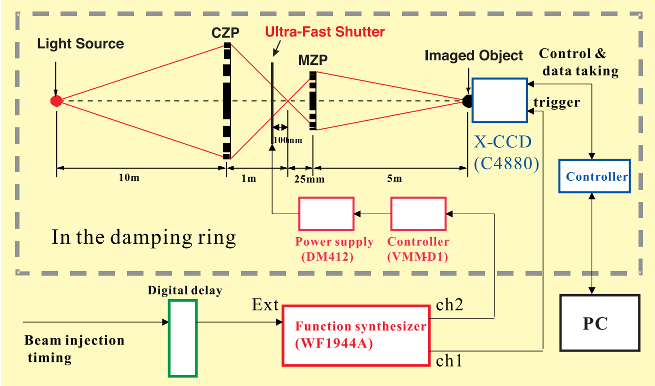

Fig. 1. Block diagram of the synchronization system with an ultra-fast shutter. This system enables the FZP beam profile monitor to have the minimum time resolution of 0.35 ms and to measure the beam profiles in synchronization with beam injection.

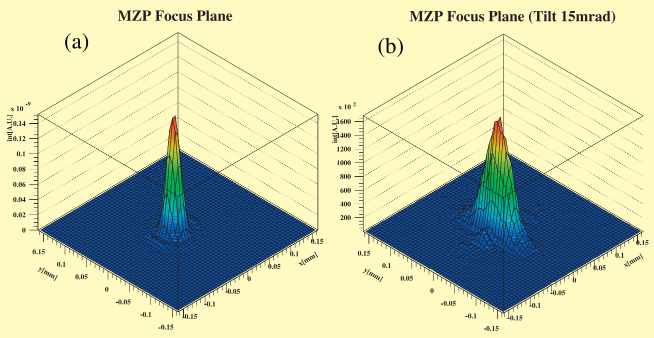

Fig. 2. Two-dimensional image profiles of an electron calculated from the Fresnel-Kirchhoff diffraction integral with the CZP tilt of (a) 0 mrad and (b) 15 mrad in the vertical direction.

alignment scheme of the optical elements could be established by utilizing the new FZP holders. The CCD background due to transmitted X-rays through the two FZPs was much reduced by an X-ray pinhole mask installed around the focus point of the CZP.

We added a system for synchronization with injection to this monitor and succeeded in obtaining the damping time with the damping wiggler on and off by measuring the beam size as function of the time after injection and confirming the effect of the damping wiggler on the damping time. Furthermore time resolution of the monitor was improved from 20 ms to 0.35 ms by installing the ultra-fast mechanical shutter around the focusing point of the CZP [3]. As a result, the influence of fast beam position fluctuation on the beam profile measurement was removed. Figure 1 shows the block diagram of the synchronization system with the ultra-fast shutter.

We developed a computer code to calculate the spatial resolution of the monitor numerically from the Fresnel-Kirchhoff diffraction integral, because the Fraunhofer approximation is invalid for the FZPs used in the monitor [4]. The spatial resolution corresponds to the image profile width of an electron moving on the orbit. The effects of the FZP alignment errors on the spatial resolution were also evaluated by using the developed computer code. Figure 2 shows the image profiles calculated with the CZP tilt of 0 and 15 mrad. The spatial resolution was calculated to be 0.5 – 0.6 μm in both vertical and horizontal directions without the FZP alignment error. The tolerable range of the alignment error for the resolution of less than 1 μm was obtained to be less than 0.6 deg. for the CZP tilt and less than 4 deg. for the MZP tilt. Since it is easy to keep the alignment error within the tolerable range, the FZP beam profile monitor has a sub-micron resolution.

References

[1] K. Iida *et al.*, Nucl. Instr. and Meth. A **506**, 41 (2003).
[2] N. Nakamura *et al.*, Proc. of the 8th EPAC, Lucerne, 2350 (2004).
[3] H. Sakai *et al.*, Proc. of the 2nd Annual Meeting of Particle Acclerator Society of Japan, 57 (2005).
[4] T. Muto *et al.*, Proc. of the 2nd Annual Meeting of Particle Acclerator Society of Japan, 21P049 (2005).

Authors

N. Nakamura, H. Sakai, T. Muto[a], and H. Hayano[a]
[a]High Energy Accelerator Research Organization (KEK)

Hydrophobic Solvation of Block Copolymer Aqueous Solutions: Pressure and Temperature Dependence

Shibayama Group

Hydrophobic interaction has been one of the most intriguing problems in physical chemistry, theoretical chemistry, and in biology. The concept of "hydrophobic bond" proposed by Kauzmann [1] is now recognized as the "hydrophobic interaction" and as one of the fundamental molecular interactions ruling the structures and functions of proteins, nucleic acids and so on. However, it is more convenient to use the term "hydrophobic solvation" when one discusses miscibility and phase behavior of aqueous systems of organic compounds, including synthetic- and bio-polymers. Block copolymers undergo microphase separation transition (MiST) due to connectivity between unlike polymer chains, *e.g.*, A and B block chains, which is characterized by a molecular-order transition. On the other hand, in the case of polymer blends and polymer solutions, a phase separation means a macrophase separation transition (MaST) because the characteristic size of phases can be infinite. Here, we report the first observation of pressure (*P*)- and temperature (*T*)-induced micro- and macro-phase separation transitions in a block copolymer solution, and discuss the role of hydrophobic solvation in the *P*-*T* plane. This system can be regarded as a prototype of protein folding.

Poly(2-(2-ethoxy)ethoxyethyl vinyl ether)-*block*-poly(2-methoxyethyl vinyl ether) diblock copolymer (pEOEOVE-pMOVE) with a narrow molecular weight distribution ($M_n = 5.7 \times 10^4$, $M_w/M_n = 1.28$) was synthesized by living cationic polymerization, where M_n and M_w are the number and weight average molecular weights, respectively [2]. The degrees of polymerization of the individual block chains, *i.e.*,

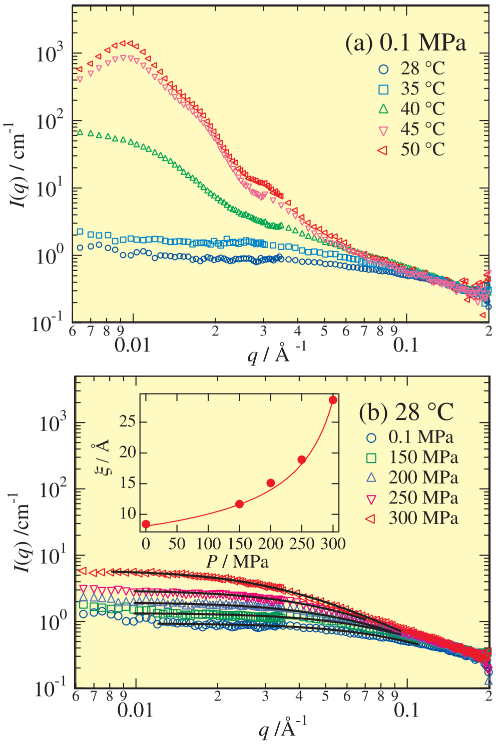

Fig. 1. SANS intensity functions, *I*(*q*)'s, of pEOEOVE-pMOVE solutions at (a) various temperatures and (b) various pressures. The solid lines in Fig. 1b denote the fit with OZ functions. The inset of Fig.1b shows the variation of the correlation length with *P*.

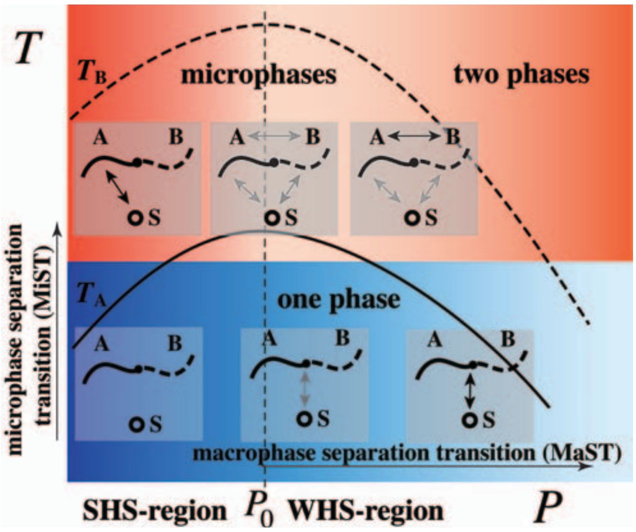

Fig. 2. Phase diagram for polyA-polyB-copolymer aqueous solutions. The solid and dashed curves denote the demixing temperatures of A, T_A (MiST) and of B, T_B (MaST). P_0 divides the strongly hydrophobic-solvated (SHS) and the weakly hydrophobic-solvated (WHS) regions. The arrows indicate repulsive interactions among A, B, and S (solvent).

pEOEOVE and pMOVE, were 200 and 400, respectively. A 15.0 wt% polymer solution was prepared by dissolving pEOEOVE-pMOVE in deuterated water (D_2O). Pressure-dependent small-angle neutron scattering (SANS) measurements were conducted at SANS-U, a small-angle neutron scattering apparatus, The University of Tokyo, Tokai, Japan. The incident wavelength was 7.0 Å and the wavelength distribution was 10 %.

At ambient pressure, the solution underwent a two-step transition at 40 and 65 ºC, both of which were convex-upward functions of P having a maximum around $P_0 \approx 150$ MPa. Fig. 1 shows SANS intensity curves, $I(q)$'s, of pEOEOVE-pMOVE solution obtained (a) at various temperatures by fixing P (= 0.1 MPa), and (b) at various pressures by fixing T (= 28 ºC). Here, q is the momentum transfer. Above 35 ºC, $I(q)$ drastically increased with increasing T, and an MiST with a bcc packing of pEOEOVE domains took place at 40 ºC. The structure grew gradually by further increasing T to 45 and 50 ºC. It is noteworthy that a reentrant MiST took place by increasing P at 45 ºC (not shown). In contrast to the temperature variation, $I(q)$ changed rather moderately with increasing P as shown in Fig. 1b and was well represented by an Ornstein-Zernike (OZ) function (solid lines). The inset shows that the correlation length, ξ, diverged at $P_{sp} \approx 350$ MPa indicating an occurrence of MaST with divergence. The experimental findings indicate the following. The pEOEOVE-pMOVE aqueous solution undergoes two types of phase transitions in P-T plane. A temperature increase at the ambient pressure resulted in MiST with a bcc structure. Pressurizing at low temperatures resulted in a MaST with a divergence of the correlation length and susceptibility. More interestingly, pressurizing at high temperatures above the MiST temperature of pEOEOVE solution exhibited a reentrant phase transition from a microphase to a new phase by way of dissolution process. It is clear from this work that the pressure effect on the hydrophobic solvation is different from temperature effect. Since a selective solvation was observed only in the low-P region, the solvation effect was found to be exclusively important at low pressures where a negative volume change by mixing is observed [3, 4]. This may be why the hydrophobic solvation plays an important role in the diversity of biological functions, such as molecular recognition and replication.

References
[1] W Kauzmann, Adv. Protein Chem. **14**, 1 (1959).
[2] S. Sugihara, S. Kanaoka, and S. Aoshima, Macromolecules **38**, 1919 (2005).
[3] I. Nasimova, T. Karino, S. Okabe, M. Nagao, and M. Shibayama, Macromolecules **37**, 8721 (2004).
[4] N. Osaka and M. Shibayama, Phys. Rev. Lett. **96**, 048303 (2006).

Authors
N. Osaka and M. Shibayama

Charge Disproportionation in β-$Na_{0.33}V_2O_5$ Revealed by Neutron Magnetic Diffraction

Hirota, Yoshizawa, and Y. Ueda Groups

A family of the β-Vanadium bronze, β-$A_{0.33}V_2O_5$ (A = Li^+, Na^+, Ag^+, Ca^{2+}, Sr^{2+}, Pb^{2+}) is a quasi-one dimensional conductor as expected from their crystal structure, which has three characteristic V chains: The V1 sites form an infinite zigzag chain of the edge-shared VO_6 octahedra, the V2 sites form a two-leg ladder of the corner-shared VO_6 octahedra, and the V3 sites form a zigzag chain of the edge-shared VO_5 pyramids. Among the family, β-$Na_{0.33}V_2O_5$ has attracted most attention because this is the first vanadium oxide to show superconductivity, which was discovered by Yamauchi *et al.* [1] under high pressures. Even more interestingly, the superconducting (SC) phase is the adjacent to the insulating (I) phase in the *PT* (pressure-temperature) phase diagram. We thus pay much attention for the nature of the I phase competing the SC phase, and the mechanism of the MI (metal-insulator) transition (T_{MI} ~ 130 K at ambient pressure) of β-$Na_{0.33}V_2O_5$ because we believe that the essential interaction can be revealed through the study of the MI transition.

Recent studies suggested the charge ordering (CO) was a possible origin of the MI transition. This picture, however, is very controversial: An x-ray diffraction study revealed the MI transition accompanied by a 6*b* lattice modulation implying a carrier localization in the V2 ladder with a period of 6*b* along the *b* axis [2], while an ESR study concluded that carriers are primarily located on the V1 sites [3]. An NMR study, on the other hand, attributed a splitting of the Knight shift at T_{MI} to the charge localization in the V1 and V2 sites [4]. In the present research [5], we have employed the

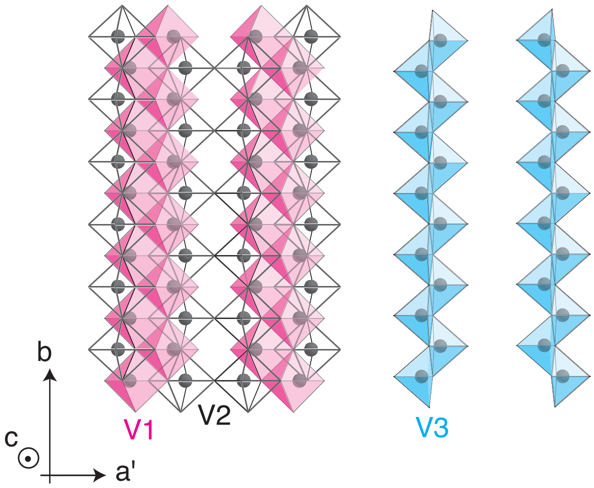

Fig. 1. Crystal structure of β-$Na_{0.33}V_2O_5$ (Monoclinic C2/*m*). V_2O_5 framework formed by $(V1)O_6$, $(V2)O_6$ and $(V3)O_6$ octahedra.

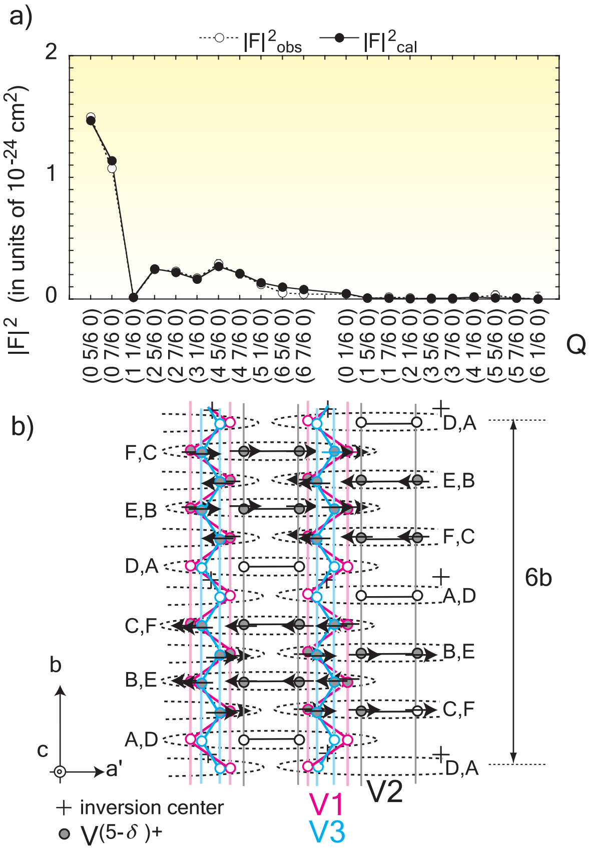

Fig. 2. Result of the least square fitting. (a) A plot of $|F|^2_{cal}$ (solid circle) vs. $|F|^2_{obs}$ (open circle). Nine parameters (six are amplitudes in the *a*' and *c* directions, three are phases) are optimized in the fitting. (b) A schematic illustration of the arrangement of magnetic moments.

neutron *magnetic* diffraction. β-$Na_{0.33}V_2O_5$ undergoes an antiferromagnetic (AF) transition at T_N ~ 24 K, which yields useful information of the charge density distribution because the spin density directly corresponds to the charge density; $S = 1/2$ and 0 correspond to V^{4+} and V^{5+} states, respectively.

Neutron diffraction experiments were performed on a single crystal of β-$Na_{0.33}V_2O_5$, grown by the Czochralski method, using the four-circle diffractometer FONDER and the triple-axis spectrometer GPTAS installed by ISSP to the JRR-3 reactor in JAEA. We have found that the magnetic Bragg reflections appear at (h, k ± 1/6, 0) with $h + k$ = odd below T_N, which indicates that the amplitude of the magnetic moments at the V sites in the *all* three types of V-O chain are modulated with a period of 3*b* along *b*. We have also confirmed that the lattice modulations occur at ~ 244 K and at ~ 131 K with a period of 2*b* and 6*b* along *b*, respectively.

Through a systematic calculation of the magnetic structure models under the constraint of the magnetic symmetry $P2_1/a$, we have concluded that the 131 K transition should be attributed to a charge disproportionation in the V 3*d* orbital with a period of 3*b*, not 6*b* as previously believed. This picture is also supported by the 3*b* periodicity in the amplitude of magnetic moments. Therefore, the 6*b* lattice modulation developing below ~131 K is attributed to an instability in the V 3*d* band to form the 3*b* charge modulation on the preexistent 2*b* lattice modulation of Na below ~244 K.

References

[1] T. Yamauchi, Y. Ueda, and N. Mori, Phys. Rev. Lett. **89**, 057002 (2002).
[2] J. Yamamura, M. Isobe, H. Yamada, T. Yamauchi, and Y. Ueda, J. Phys. Chem. Solids **63**, 957 (2002).
[3] M. Heinrich, H.-A. Krug von Nidda, R.M. Eremina, A. Loidl, Ch. Helbig, G. Obermeier, and S. Horn, Phys. Rev. Lett. **93**, 116402 (2004).
[4] M. Itoh, N. Akimoto, H. Yamada, M. Isobe, and Y. Ueda, J. Phys. Chem. Solids **62**, 351 (2001).
[5] S. Nagai, M. Nishi, K. Kakurai, Y. Oohara, H. Yoshizawa, H. Kimura, Y. Noda, B. Grenier, T. Yamauchi, J. Yamaura, M. Isobe, Y. Ueda, and K. Hirota, J. Phys. Soc. Jpn. **74**, 1297 (2005).

Authors

S. Nagai, M. Nishi, K. Kakurai[a], Y. Oohara, H. Yoshizawa, H. Kimura[b], Y. Noda[b], B. Grenier[c], T. Yamauchi, J. Yamaura, M. Isobe, Y. Ueda, and K. Hirota
[a]Japan Atomic Energy Agency
[b]IMRAM, Tohoku University
[c]CEA-Grenoble, France

Structures and Low-energy Excitations of Amorphous Clathrate Hydrates

Yamamuro Group

Clathrate hydrates are well-known inclusion compounds which accommodate various guest molecules in their cage-like structures formed by water molecules. There are two major structural types: type I (space group: Pm3n) and type II (Fd3m) depending on the van der Waals diameter of guest molecule; molecules larger than 0.55 nm and smaller than 0.40 nm prefer type II. The ideal compositions of type I and II hydrates are $M\cdot5.75H_2O$ and $M\cdot17H_2O$, respectively. Recently, natural methane hydrate deposited under seabed is remarked as future energy resource and various applications using clathrate hydrates (*e.g.*, molecular sieves, heat reservoir, etc.) are studied actively. From the basic scientific point of view, however, the clathrate hydrates have been important materials as exotic disordered crystals (both guest and water orientations are disordered) and model systems of hydrophobic hydration for a long time.

Recently, we found that amorphous clathrate hydrates are realized by vapor-deposition technique and they exhibit interesting low-energy phonon excitations [1,2]. We chose Ar (0.38, II), CD_4 (0.41, I), Xe (0.44, I) and SF_4 (0.58, II) as guest molecules to investigate their size dependence; the numbers in the parentheses denote average van der Waals diameter in nm and structural type. The amorphous samples were prepared in a novel cryostat designed for *in-situ* neutron scattering measurements [3,4]. The mixed gas of the guest and water vapor was deposited slowly on a substrate at ca. 10 K. The mass of the deposited sample was ca. 0.5 cm^3

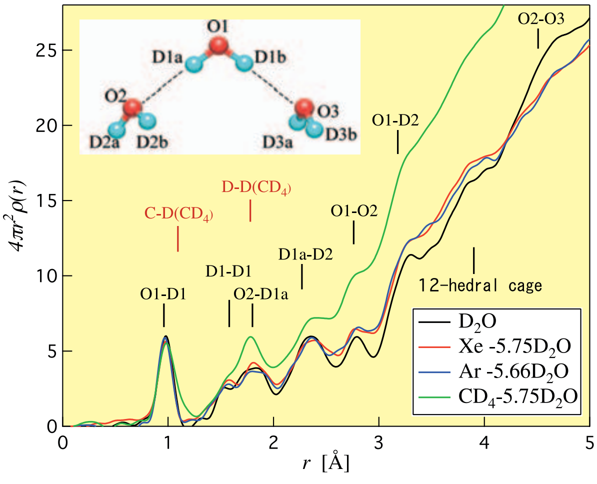

Fig. 1. Radial distribution functions calculated from the neutron diffraction data of vapor-deposited amorphous $Xe\cdot5.75D_2O$, $Xe\cdot17D_2O$, $CD_4\cdot5.75D_2O$ and D_2O. The tick marks denote the atomic distances for the three adjacent D_2O molecules in the figure.

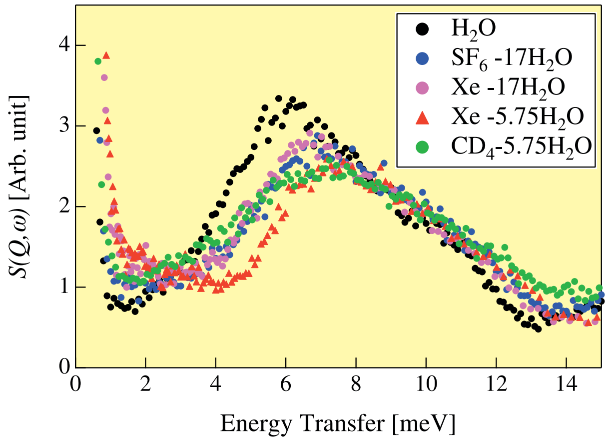

Fig. 2. Dynamic structure factors of vapor-deposited amorphous Xe·5.75H_2O, Xe·17H_2O, CD_4·5.75H_2O, SF_6·17H_2O and H_2O.

corresponding to a thickness of 0.13 mm. Their neutron diffraction and inelastic neutron scattering data were measured by HIT and LAM-D spectrometers (both at KEK), respectively. The data of as-deposited sample were collected first and then the samples annealed at 120 K and 150 K were measured to investigate the effects of structural relaxation and crystallization.

Figure 1 shows the radial distribution functions of the three vapor-deposited hydrates and D_2O. The all of intramolecular and intermolecular atomic correlations were reproduced well. The RDF's of the amorphous Xe and Ar hydrates are considerably larger than that of amorphous D_2O around 4 Å corresponding the center-to-wall distance of the 12-hedral hydrate cage; the RDF of CD_4 hydrate is larger than others because a CD_4 molecule consists of five atoms. The present result indicates that local cage-like structure is kept even in the amorphous solids.

Figure 2 shows the incoherent inelastic neutron scattering data. The peak of amorphous H_2O around 7 meV is due to the acoustic mode and the intensity below 7 meV is sensitive for annealing condition. Therefore it is believed that excess density of states, sometimes called boson peak, exists below 7 meV for amorphous H_2O. The intensity below 7 meV was clearly reduced by adding guest molecules, depending on the concentration and size of the guests. This may be due to the fact that the hydrogen-bond formation is promoted and disorder, defects and distortion of amorphous structure, which might be related to the origin of the boson peak, were reduced by adding guest molecules with large hydrophobic hydration effect. It is also of interest that excess excitation appeared below 3 meV for amorphous hydrates. This may be related to the cooperative motion of the cage and guest molecules but further details of the origin are unknown. We are now planning the experiments on the amorphous hydrate of H_2 (or D_2) which is the smallest guest molecule.

References

[1] O. Yamamuro, T. Matsuo, I. Tsukushi, and N. Onoda-Yamamuro, Can. J. Phys. **81**, 107 (2003).
[2] O. Yamamuro, Y. Inamura, and N. Onoda-Yamamuro, Physica B, (2006) in press.
[3] O. Yamamuro, Y. Madokoro, H. Yamasaki, T. Matsuo, I. Tsukushi, and K. Takeda, J. Chem. Phys. **115**, 9808 (2001).
[4] O. Yamamuro, T. Matsuo, N. Onoda-Yamamuro, K. Takeda, H. Munemura, S. Tanaka, and M. Misawa, Europhys. Lett. 63, **368** (2003).

Authors

O. Yamamuro, T. Kikuchi, Y. Inamura[a], and N. Onoda-Yamamuro[b]
[a]Japan Atomic Energy Agency
[b]Tokyo Denki University

E/T-scaling Behavior of Spin Fluctuations in the p-Zn-Mg-Ho Quasicrystal

Sato Group

Quasicrystals have distinct spatial symmetry characterized by highly-ordered but non-periodic atomic arrangement. This special atomic structure, called *quasiperiodic structure*, has hidden translational symmetry in higher dimensional space, and thus differs both from the periodic crystals and random glasses.

Since the discovery of the quasicrystals in 1984 [1], extensive efforts have been made to understand their structure and physical properties. Ordering and dynamics of magnetic moments (spins) in the quasiperiodic structures have been one of fundamental topics to date. Theoretically, a number of interesting phenomena are expected, such as non-collinearly ordered ground state with hierarchical spin-fluctuation distribution [2], nevertheless, earlier experimental studies only detected rather normal behavior; most of the magnetic quasicrystals exhibit typical spin-glass-like behavior in macroscopic susceptibility, suggesting random freezing of spins. Using the neutron scattering technique, we have revealed several non-trivial features in the spin ordering and dynamics in magnetic quasicrystals, such as significant short-range order with localized collective modes in the Zn-Mg-Tb quasicrystal [3]. Here, we will give a brief summary of our recent discovery --temperature independent spin excitation spectrum--, which is, we believe, the most prominent feature ever found in the magnetic quasicrystals.

Figure 1 shows the magnetic excitation spectra at several temperatures from 1.4 K to 200 K, observed using a powder sample of the p-type Zn-Mg-Ho quasicrystals. The experiment was carried out using LAM-40 inverted-geometry time-of-flight spectrometer installed at KEK. One may immediately notice that the scattering intensity for the neutron-energy-loss side ($\hbar\omega > 0$) is mostly temperature independent. This surprising independence can never be an experimental fault, since the energy-gain side ($\hbar\omega < 0$) shows usual temperature dependence. Neutron scattering cross-section for spin systems may be given in terms of dynamic susceptibility as:

$$S(Q,\hbar\omega,T) \propto [1+n(\hbar\omega,T)]\,\mathrm{Im}\chi(Q,\hbar\omega,T),$$

and thus, the temperature-independence requires a special function form in $\mathrm{Im}\chi(Q,\hbar\omega,T)$, which compensates the usual Bose-temperature factor term $[1+n(\hbar\omega,T)]$. After several trials, we found that the spectrum in $0.2 < \hbar\omega < 1.5$ meV can be well described by the following function in

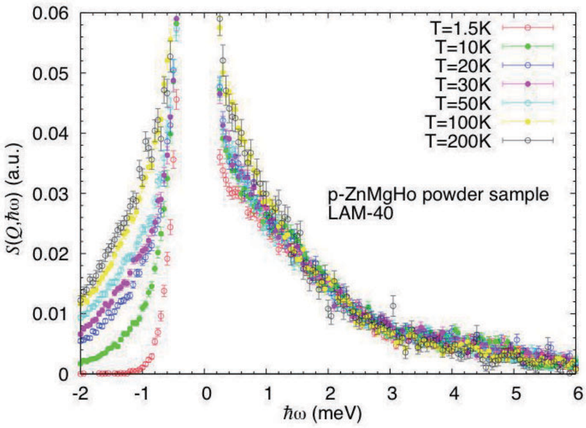

Fig. 1. Inelastic excitation spectra in the p-type Zn-Mg-Ho quasicrystal at several temperatures ranging from 1.5 K to 200 K. Scattering angle was fixed to 24.3 deg.

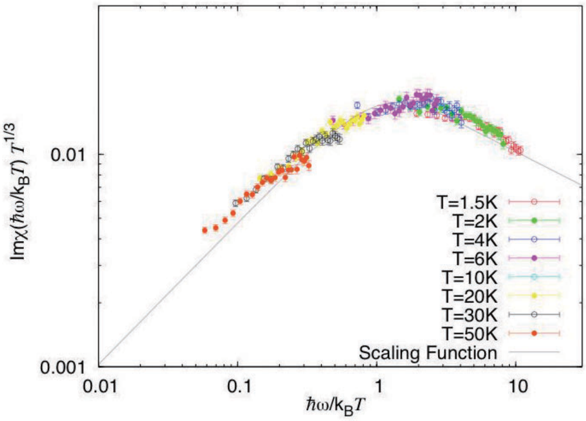

Fig. 2. Imaginary part of the dynamic susceptibility (with weak prefactor $T^{1/3}$) scaled by $\hbar\omega/k_B T$. Solid line shows the scaling function with $\alpha = 1.00(2)$. See text for details.

entire temperature range:

$$\mathrm{Im}\chi(Q,\hbar\omega,T) \propto (\hbar\omega)^{-1/3}\tanh(\alpha\hbar\tilde{\omega}/k_B T),$$

which has similar $\hbar\omega$- and T-dependence as the inverse of the Bose temperature factor. This form of the dynamic susceptibility further suggests a scaling law:

$$\mathrm{Im}\chi(Q,\hbar\tilde{\omega}/k_B T)(k_B T)^{1/3} \propto (\hbar\omega/k_B T)^{-1/3}\tanh(\alpha\hbar\tilde{\omega}/k_B T).$$

This is a typical *E/T*-scaling function, where the susceptibility is scaled only by *E/T*, except for the weak prefactor $T^{1/3}$. This *E/T*-scaling is frequently observed in the non-Fermi-liquid (NFL) compounds, such as UCu_4Pd [4]. Several mechanisms have been proposed to understand this *E/T*-scaling in the NFL compounds, such as the local quantum criticality or the disordered quantum Griffiths singularity. At the present moment we are not sure what mechanism is responsible for the *E/T*-scaling in the magnetic quasicrystal, however, we believe there must be interesting common background in the two seemingly different systems.

References

[1] D. Shechtman *et al.*, Phys. Rev. Lett. **53**, 1951 (1984).
[2] S. Wessel *et al.*, Phys. Rev. Lett. **90**, 177205 (2003).
[3] T. J. Sato, Acta Crystallogr. **61**, 39 (2005); T. J. Sato *et al.*, Phys. Rev. B **73**, 054417 (2006).
[4] M. C. Aronson *et al.*, Phys. Rev. Lett. **75**, 725 (1995).

Authors

T. J. Sato and A. P. Tsai[a]
[a]IMRAM, Tohoku University

Spin-Flop Multicritical Phenomena in Mn_2AS_4 (A = Si and Ge)

Y. Ueda Group

We have succeeded in elucidating anomalous magnetic properties of Mn_2AS_4 (A = Si and Ge) by combining the magnetic field-temperature (*H-T*) phase diagram associated with spin-flop transition and the representation analysis of magnetic structures [1].

Figures 1(a)-1(c) represent temperature dependence of the magnetization (*M*) divided by the external magnetic field (*H*) for various magnetic fields for A = Si. As clearly seen in Fig. 1(c), weak ferromagnetism along the *c*-axis with a spontaneous magnetic moment of 0.042 μ_B/Mn^{2+} emerges in a very narrow temperature range just below Néel temperature (T_N = 86 K). On the other hand, the *M*/*H* along the *b*-axis at 0.1 T steeply decreases with lowering temperature, which indicates a uniaxial anisotropy with the *b*-direction as an easy axis. This feature is more clearly seen in *M-H* curves as a spin-flop transition. By taking isothermal magnetization curves at various temperatures, we obtain a *H-T* phase diagram associated with spin-flop transition (Fig. 1(g)). Compared with conventional uniaxial antiferromagnets, the peculiar feature of the phase diagram is that the spin-flop field (H_{SF}) shows a steep decrease near T_N and the first-order line of the spin-flop transition meets the H = 0 line at a certain temperature *T'* (~ 83.5 K). If we assume that the spin easy axis varies from the *b*- to *a*-axis upon the spin-flop transition without a change of the pattern of spin arrangements (C_i-C'_i ; i = a, b, and c), the observed weak ferromagnetism can be well understood; the irreducible representation related to C_b-C'_b type spin arrangements has neither F_i nor F'_i type component, whereas the irreducible representation responsible for C_a-C'_a type spin arrangements includes both F_c and F'_c type component (ferromagnetism along the *c*-axis).

The system of A = Ge exhibits essentially similar temperature dependence of *M*/*H* to A = Si case (Fig. 1(d)-1(f)). However, there are several differences. A careful examination of *M-H* curve at 86 K tells us that spontaneous weak ferromagnetism does not appear near T_N, but *M*/*H* along the *c*-axis shows merely an enhancement under small magnetic field near T_N. Another difference is that *M*/*H* along the *a*-axis shows an enhancement at low temperatures, which is not discernible in A = Si. These two characteristics are also understood through a phase diagram (Fig. 1(h)). In marked contrast to A = Si, the first-order line does not meet the H = 0

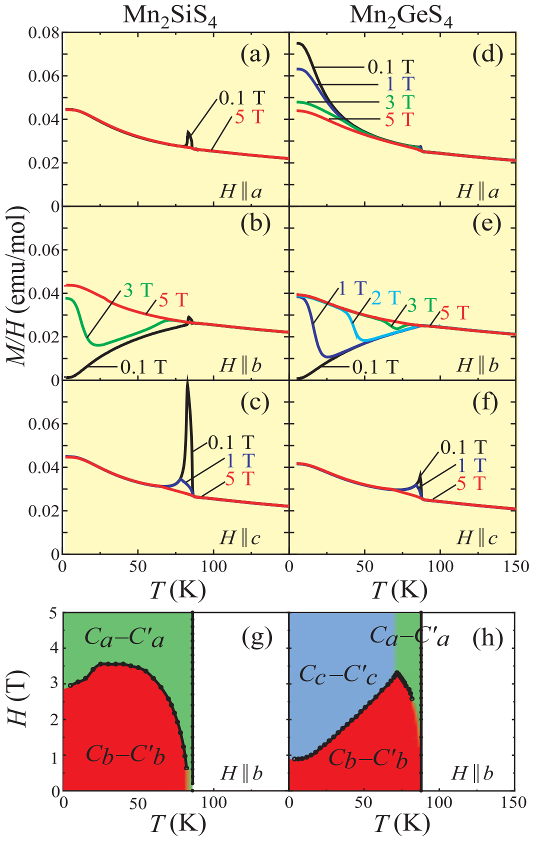

Fig. 1. (a)-(f) Temperature (*T*) dependence of the magnetization (*M*) divided by the external magnetic field (*H*) at various magnetic fields along the *a*- [(a) and (d)], *b*- [(b) and (e)], and *c*-axes [(c) and (f)] for Mn_2SiS_4 [(a)-(c)] and Mn_2GeS_4 [(d)-(f)]. *M* is detected along the same direction as *H*. (g), (h) The magnetic field-temperature (*H-T*) phase diagram for Mn_2SiS_4 (g) and Mn_2GeS_4 (h). *H* is applied along the *b*-axis. The C_i-C'_i (i = a, b, and c) denote antiparallel arrangements of each ferromagnetic chains with each spin parallel to the *i*-th axis. The phase boundaries between the paramagnetic and magnetic phases represent the second order transition, whereas those between different types of magnetic phases indicate the first order spin-flop transition.

line, but it terminates as a bicritical point on the second-order line of antiferromagnetic transition. The enhancement of M/H along the c-axis near T_N is most likely a reflection of fluctuations of C_a-C'_a type spin arrangements, which can be stabilized by the application of small magnetic field. We can explain the enhancement of M/H along the a-axis in a similar manner by assuming that the spin easy axis is the c-axis in the spin-flopped phase at low temperatures; both F_a and F'_a type components belong to the same irreducible representation as C_c-C'_c type spin arrangements, which fluctuations can be observed even at zero magnetic field owing to a smallness of H_{SF}. The boundary between C_a-C'_a and C_c-C'_c type spin arrangements may be a first-order line, however, its location in the H-T plane is unclear at present.

We need further studies to pursue intriguing aspects of present compounds, for example, (1) what kind of microscopic scenario takes part in a sudden decrease of H_{SF} near T_N; (2) what is the criticality of the phase transition at the unusual multicritical point, where first-order lines and second-order lines converge on the $H = 0$ line.

References

[1] K. Ohgushi and Y. Ueda, Phys. Rev. Lett. **95**, 217202 (2005).

Authors

K. Ohgushi and Y. Ueda

Crystal Growth of 3d Heavy Fermion Compound, LiV_2O_4

Y. Ueda Group

Normal spinel oxides show a rich variety of electromagnetic properties which are closely related to the strong geometrical frustration of a three-dimensional network with corner-sharing magnetic tetrahedra, the so-called pyrochlore lattice. LiV_2O_4 with a mixed valence of V^{3+} and V^{4+} is also a member of spinel oxides and very interestingly shows heavy fermion behavior despite its d-electron system. The mechanism of such heavy fermion behavior in LiV_2O_4 has not been resolved, partly owing to the lack of high-quality single crystals. We succeeded in growing single crystals of LiV_2O_4 using an effective solvent system for mixed-valence vanadium (V^{3+} and V^{4+}) oxides [1]. We selected a LiCl-Li_2MoO_4-$LiBO_2$ system with 69:26:5 molar ratio, as a flux. The pellet of polycrystalline LiV_2O_4 with flux materials was put into a platinum crucible with a carbon lid and loaded into a fused quartz tube, the inside of which was coated with a carbon film formed by pyrolysis of acetone, thus avoiding tube breakage by reaction with lithium compounds. The tube was sealed under a 10^{-4} torr atmosphere and then placed in a furnace. The best growth condition at 1:1 ratio of LiV_2O_4/flux was as follows: the sample was soaked at 800°C for 10 h, cooled to 450°C in 72 h and then cooled to room temperature in 10 h. The grown crystals have a well-developed octahedral form bounded by {111} faces, with high crystallographic quality and maximum size of almost 1.0-1.0-1.0 mm, as shown in Fig. 1. The crystals have stoichiometric composition and show heavy fermion behavior with an extremely large γ value of ~460 mJ mol^{-1} K^{-2}.

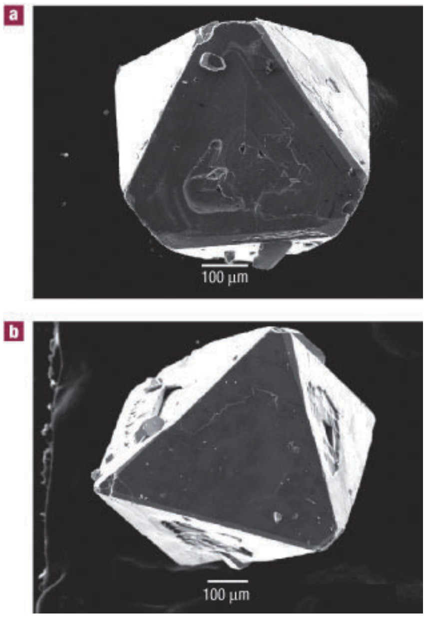

Fig. 1. Scanning electron micrograph of grown LiV_2O_4 single crystals with 1.0 × 1.0 × 1.0 mm size in the cross edge direction.

By using thus grown crystals, various measurements were done. A sharp peak structure in the density of states at ~4 meV above the Fermi level (E_F) was observed in a vacuum ultraviolet laser excited photoemission spectroscopy [2]. The evolution of the peak height corresponds well with the crossover behavior to the heavy-fermion-like state as observed in the thermal and transport properties. The position, shape, and temperature dependence of the peak structure is quite similar to the Kondo resonance observed in conventional f-electron heavy Fermion compounds. On the other hand, the muon Knight shift measured in single crystals of LiV_2O_4 strongly suggests that the anomalous properties of LiV_2O_4 originate from frustration of local magnetic moments [3]; the presence of inhomogeneous local magnetic moments is demonstrated by the broad distribution of the Knight shift at temperatures well below the presumed Kondo temperature ($T^* \simeq 30$ K) and moreover, a significant fraction ($\simeq$ 10 %) of the specimen gives rise to a second component which is virtually non-magnetic.

References

[1] Y. Matsushita, H. Ueda, and Y. Ueda, Nature Materials **4**, 845 (2005).
[2] A. Shimoyamada, S. Tsuda, K. Ishizaka, T. Kiss, T. Shimojima, T. Togashi, S. Watanabe, C. Q. Zhang, C. T. Chen, Y. Matsushita, H. Ueda, Y. Ueda, and S. Shin, Phys. Rev. Lett. **96**, 026403 (2006).
[3] A. Koda, R. Kadono, K. Ohishi, S.R. Saha, W. Higemoto, Y. Matsushita and Y. Ueda, J. Phys.: Condens. Matter **17**, L257 (2005).

Authors

Y. Matsushita, H. Ueda, and Y. Ueda

A New Spin-1/2 Dimer System $Ba_3Cr_2O_8$ with Rare Cr^{5+}

Y. Ueda Group

$Ba_3Mn_2O_8$ with the valence state of Mn^{5+} ($3d^2$, $S = 1$) has drawn much interest in its gapped ground state and magnetization plateau at half of saturated magnetization [1]. The crystal structure is made up of isolated tetrahedral MnO_4^{3-} and Ba^{2+} ions, where Mn^{5+} ions set up double-layered triangular lattices which are stacked along the c-axis with threefold periodicity, as shown in the inset of Fig.1. The antiferromagnetic intradimer interaction J_0 (see Fig. 1) is dominant, which is the origin of the spin gap. Moreover, the interdimer interactions J_1, J_2 and J_3 are also antiferromagnetic and their total is almost equivalent to a magnitude of J_0.

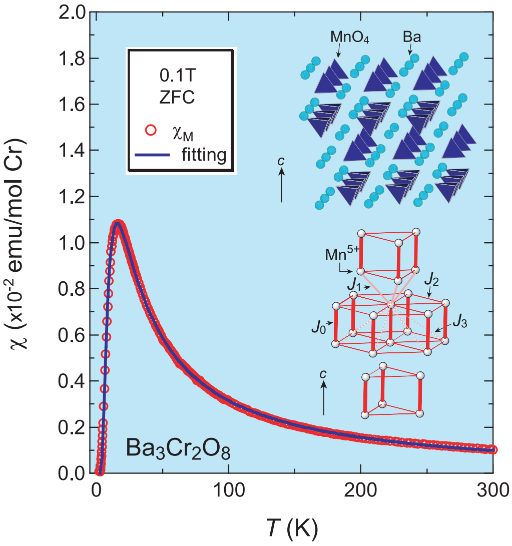

Fig. 1. Temperature dependence of magnetic susceptibility for $Ba_3Cr_2O_8$. The circles and line are the observed and calculated magnetic susceptibility, respectively. The inset shows the crystal structure and magnetic interactions.

We have successfully synthesized the isostructural compound, $Ba_3Cr_2O_8$ with very rare Cr^{5+} ($3d^1$, $S = 1/2$) and the compound was found to be a three-dimensional quantum spin system with a spin singlet ground state of dimer origin [2]. From the analysis of magnetic susceptibility (χ) and high-field magnetization data, excitation gap is evaluated as $\Delta/k_B = 16.1$ K. The calculated χ well reproduces the observed χ in the temperature range of 6 ~ 300 K, as shown in Fig. 1. The parameters obtained from the best-fit are $g = 1.975(6)$, $J_0/k_B = 25.04(3)$ K, $J'(= 3J_1 + 6J_2 + 6J_3)/k_B = 7.69(9)$ K and $\chi_0 = -1.9(2) \times 10^{-4}$ emu/mol. Thus, $Ba_3Cr_2O_8$ can be regarded as a coupled antiferromagnetic dimer system similar to $Ba_3Mn_2O_8$, where the interdimer interactions work effectively. The obtained interactions of $Ba_3Cr_2O_8$ are stronger (weaker) in the intradimer (interdimer) than those of $Ba_3Mn_2O_8$; $J_0/k_B = 17.4$ K and $J'/kB = 24.9$ K. Because it is thought that the magnitudes of intra- and interdimer interactions are proportional to their corresponding distances d_{Ji}, we compare d_{Ji} between $Ba_3Cr_2O_8$ ($d_{J0} = 3.934$ Å, $d_{J1} = 4.599$ Å, $d_{J2} = 5.739$ Å and $d_{J3} = 6.958$ Å) and $Ba_3Mn_2O_8$ ($d_{J0} = 3.984$ Å, $d_{J1} = 4.569$ Å, $d_{J2} = 5.711$ Å and $d_{J3} = 6.963$ Å). d_{J0} related to the intradimer interaction is shorter by 1.27 % in $Ba_3Cr_2O_8$, whereas in the interdimer interactions, d_{J1} and d_{J2} are longer by 0.65 % and 0.49 %, respectively, and d_{J3} is shorter by 0.07 % in $Ba_3Cr_2O_8$ than those in $Ba_3Mn_2O_8$. These results suggest that $Ba_3Cr_2O_8$ has a stronger intradimer interaction and weaker interdimer interactions than those of $Ba_3Mn_2O_8$, which are in agreement with the results obtained from the analysis of magnetic susceptibility.

References

[1] M. Uchida, H. Tanaka, M. I. Bartashevich, and T. Goto, J. Phys. Soc. Jpn. **70**, 1790 (2001); M. Uchida, H. Tanaka, H. Mitamura, F. Ishikawa, and T. Goto, Phys. Rev. B **66**, 54429 (2002).
[2] T. Nakajima, H. Mitamura, and Y. Ueda, J. Phys. Soc. Jpn. **75**, 054706 (2006).

Authors
T. Nakajima, H. Mitamura, and Y. Ueda

'From-Edge-to-Interior' Spin Freezing in a Magnetic Dipolar Cube

Takayama Group

In recent years, systems consisting of arrayed ferromagnetic nanoparticles have attracted much attention as a possible element with a high storage density. To understand magnetic properties of such systems the dipole-dipole interaction is considered to be important as well as the magnetic anisotropic energy of each nanoparticle moment. The former interaction has been well known since long ago, but cooperative aspects of dipolar systems, *i.e.*, those of spins interacting only via the dipole-dipole interaction, have little investigated [1]. This is particularly the case for dipolar systems of a finite size. We have recently investigated various finite-size dipolar systems whose magnetic dipole moments are represented by classical Heisenberg spins, $\mathbf{S}_i$'s.

Let us discuss here a dipolar cube, which is cut out from a simple cubic lattice with the edges in parallel to the lattice axes. The corresponding bulk dipolar system has the ground state with the global continuous O(3) symmetry (see Fig. 1a), or it is given by any linear combination properly normalized of x-, y-, and z-antiferromagnetically aligned ferromagnetic chains (af-FMC) orders where the last one is shown in Fig. 1b [1]. We have investigated the freezing behavior of the diploar cube during cooling process by the standard molecule dynamics simulation, and have found a peculiar finite size effect, which we call '*from-edge-to-interior*' freezing [2]. Figure 2 shows patterns of the local freezing parameters, S_i's, the magnitudes of the time-averaged $\mathbf{S}_i$'s, which represent the degree of freezing of each spins. At T=0.625 (a), a little higher than T* at which the system's specific heat C exhibits a rather sharp peak, spins on some edges start freezing. As T further decreases, the freezing extends from edges to the interior and spins form domains (b-d), each of which is in one of the three af-FMC orders whose ferromagnetic alignment is in parallel to the edge. The ground state consists of 12 domains extending from the edges as shown in Fig. 1c.

We attribute a possible origin of the peculiar freezing process described above to the reduction of symmetry of the interaction Hamiltonian from $O(3)$ in bulk (or interier) to Z_2 on edges. In the interior, short-ranged orders with the continuous $O(3)$ symmetry change easily their order as a whole. On the edges, on the other hand, the symmetry is broken into the Z_2 due to the peculiar anisotropic nature of the dipole-dipole interaction, which connects the anisotropy in the spin space with that in the real space, combined with the existence of the boundary. The consequence is a free-energy barrier of the order of the system linear dimension L against an overturn of ferromagnetically aligned spins on the edge.

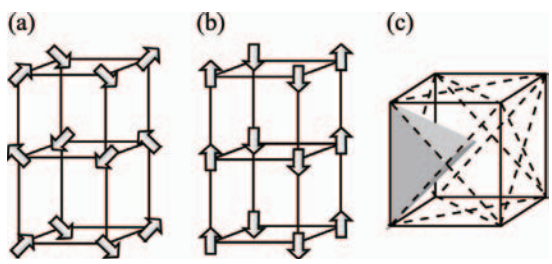

Fig. 1. Spin configurations in the ground state. (a) One of the bulk orders, (b) the z-af-FMC order, and (c) the 12-domain structure in low energy states of the dipolar cube.

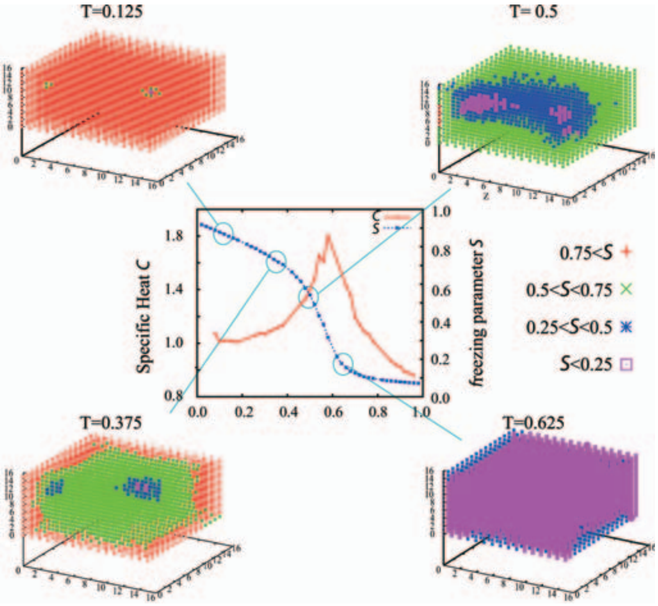

Fig. 2. Freezing patterns S_i's of the dipolar cube with L=16 at temperatures indicated whose unit is a characteristic magnitude of the dipole-dipole interaction of interest. The system's specific heat C and order parameter parameter S representing the degree of the bulk $O(3)$ symmetry are shown in the center.

So far we have described the role of the peculiar anisotropic nature of the dipole-dipole interaction on the magnetic properties of a dipolar cube. This anisotropic feature is apparently concentrated near the boundaries, or of short-ranged in nature. We have to mention, however, that the long-ranged nature of the interaction is indispensable for the system to reach the lowest-energy multi-domain state [2]. Similar as well as different types of boundary-dependent magnetic orderings are observed in finite dipolar systems cut out from FCC and HCP lattices and from a 2-dimensional square lattice.

References
[1] J. M. Luttinger and L. Tisza, Phys. Rev. **70**, 954 (1946).
[2] K. Matsushita *et al*, J. Phys. Soc. Jpn. **74**, 2651 (2005).

Authors
K. Matsushita, R. Sugano[a], A. Kuroda, Y. Tomita, and H. Takayama.
[a]Advanced Research Laboratory, Hitachi Ltd.

Tree Approximation for Spin Glass Models

Kawashima Group

The spin glass problem was brought forth by experiments on random magnets, and the Edwards-Anderson model was subsequently proposed. Since then, the simplicity of the model and the fundamental nature of the problem have been encouraging a great deal of effort to be invested on its study. While the existence of the spin-glass phase transition was established by Monte Carlo simulations [1], the nature of the spin glass phase is a subject of active debates even today. Early theoretical works produced two paradigms that are consistent with experimental findings: the mean-field picture and the droplet picture. Investigations in the last two decades have been focused on the question as to which paradigm is correct for the three-dimensional model. For solving this problem, the principal tool was numerical calculations. It did not take too long, however, for researchers to realize the difficulty of the problem from the computational point of view. Even a mathematically rigorous statement was made: the problem of finding the ground-state of a given sample of the Edwards-Anderson spin glass model is NP-hard if the lattice is three dimensional or higher. Today's largest system size that can be handled with conventional methods does not exceed L=30 for three-dimensional models, which is not enough to answer the question beyond reasonable doubts.

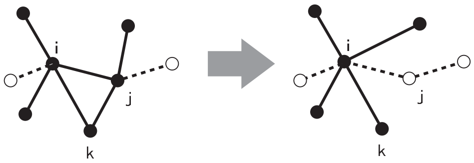

Fig. 1. A contraction process. Circles are vertices (or spins) and lines are edges (or bonds). Solid lines are those which have not been contracted yet and dashed lines are the ones that have been contracted already.

We here propose another way of approaching the problem [2]. Namely, we discuss an approximate numerical method. One of the most well-known examples for methods of this kind is the Migdal-Kadanoff (MK) real space renormalization, which yields a reasonably accurate result for the ferromagnetic Ising model and was applied later to spin glasses. The MK method yields results that support the droplet picture against the mean-field picture. Our approximation procedure consists of repeated application of an elementary operation ("*contraction*") to the model with a given lattice geometry and the system size. As depicted in Fig.1, a contraction is performed as reconnection of bonds and recalculation of the bond strength. Starting from the graph of the same structure as the finite lattice on which the model is defined, we gradually deform the graph by contraction until it becomes a tree with no loop. Once the lattice has been deformed into a tree, it is easy to compute the correlation functions because of the absence of loops. In this way, we can treat much larger systems than we can with conventional numerical methods such as the Monte Carlo simulation.

For the three dimensional system, the spin glass susceptibility shows a drastic change near T=J, which is presumably

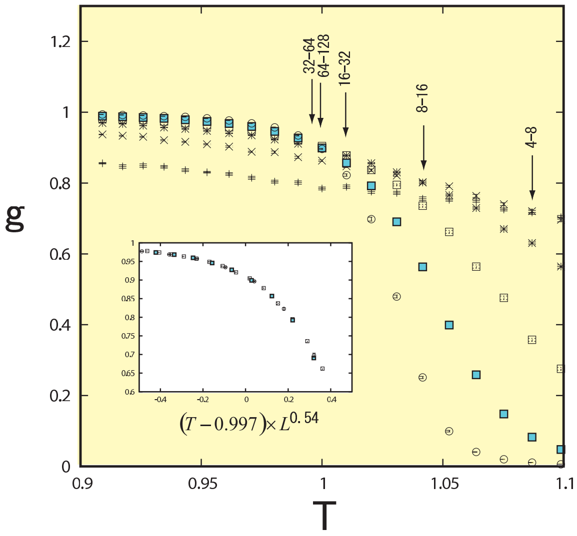

Fig. 2. The Binder parameter for the three-dimensional model of system sizes of L=4, 8, 16, 32, 64 and 128 (from top to bottom at high temperature). The arrows indicate the locations of the crossings between two successive system sizes. The inset shows the finite size scaling for the largest three sizes, L= 32, 64 and 128. (The other sizes are not shown in the inset.)

the transition temperature. This is confirmed by Fig.2, which shows the temperature dependence of the Binder parameter and the finite-size-scaling plot based on it. Curves of various system sizes cross each other and the crossing between larger systems takes place at lower temperature. The crossing point in the thermodynamic limit is located around $T = 1.0\ J$ and $g = 0.9$. We can also produce a finite-size-scaling plot that looks reasonable, as shown in the inset. The plot yields the estimates of the critical exponent; $\nu=1.85$. The agreement of these values with the results of Monte Carlo simulation [3], $T_c = 0.98(5)$ and $\nu= 2.00\ (15)$, are remarkably good considering that the crudeness of the present approximation. This is also an improvement on the MK result [4], $T_c = 0.39$ and $\nu=2.8$.

The variance of the distribution of the squared overlap, q^2, is also computed. The variance is a decreasing function of the system size at any temperature. The decrease is rapid both at the high and low temperature ranges and is somewhat more moderate in the middle. However, even at the middle range, the variance is extremely small and converges to zero in the thermodynamic limit, which suggests that the overlap distribution function $P(q)$ has a trivial structure, consistent with the droplet picture.

References

[1] N. Kawashima and A. P. Young, Phys. Rev. B **53**, R484 (1996).
[2] N. Kawashima, J. Phys. Soc. Jpn. **25**, (2006) in press.
[3] E. Marinari, G. Parisi and J. J. Ruiz-Lorenzo, Phys. Rev. B **58**, 14852 (1998).
[4] B. W. Southern and A. P. Young J. Phys. C **10**, 2179 (1977).

Authors
N. Kawashima